International Journal of Heat and Mass Transfer 88 (2015) 55–72

Contents lists available at ScienceDirect

International Journal of Heat and Mass Transfer

journal homepage: www.elsevier.com/locate/ijhmt

Modeling of the non-isothermal liquid droplet impact on a heated solid substrate with heterogeneous wettability

Sashikumaar Ganesan *, Jagannath Venkatesan, Sangeetha Rajasekaran

Numerical Mathematics and Scientific Computing, SERC, Indian Institute of Science, Bangalore 560 012, India

ARTICLE INFO

Article history:
Received 20 June 2014
Received in revised form 14 April 2015
Accepted 15 April 2015

Keywords:
Droplet impingement
Heterogeneous wettability
Heat transfer
Marangoni convection
Finite elements
ALE approach

ABSTRACT

A comprehensive numerical investigation on the impingement and spreading of a non-isothermal liquid droplet on a solid substrate with heterogeneous wettability is presented in this work. The time-dependent incompressible Navier–Stokes equations are used to describe the fluid flow in the liquid droplet, whereas the heat transfer in the moving droplet and in the solid substrate is described by the energy equation. The arbitrary Lagrangian–Eulerian (ALE) formulation with finite elements is used to solve the time-dependent incompressible Navier–Stokes equation and the energy equation in the time-dependent moving domain. Moreover, the Marangoni convection is included in the variational form of the Navier–Stokes equations without calculating the partial derivatives of the temperature on the free surface. The heterogeneous wettability is incorporated into the numerical model by defining a space-dependent contact angle. An array of simulations for droplet impingement on a heated solid substrate with circular patterned heterogeneous wettability are presented. The numerical study includes the influence of wettability contrast, pattern diameter, Reynolds number and Weber number on the confinement of the spreading droplet within the inner region, which is more wettable than the outer region. Also, the influence of these parameters on the total heat transfer from the solid substrate to the liquid droplet is examined. We observe that the equilibrium position depends on the wettability contrast and the diameter of the inner surface. Consequently, the heat transfer is more when the wettability contrast is small and/or the diameter of inner region is large. The influence of the Weber number on the total heat transfer is more compared to the Reynolds number, and the total heat transfer increases when the Weber number increases.

1. Introduction

The dynamic behavior of droplets and sprays impinging on a solid substrate is of great importance in many industrial applications such as spray cooling, spray forming, flow boiling, ink-jet printing, thermo-syphons, fuel injection, engines with internal combustion and jet impingement cooling. Most of the industrial applications involve droplets or spray impact on solid substrate with heat transfer and phase change, which are mainly influenced by the droplet dynamics. The spray-wall interactions and the heat transfer process are very complex and our understanding is far from being complete. The insight into the fundamental mechanisms responsible for the wetting and heat transfer in two-phases is indispensable for optimal results and therefore scientific studies on single droplet impact on hot solid substrate, including heterogeneous wettability are highly demanded.

Although investigations involving a droplet wetting on non-homogenous surfaces are in the early stages of research, droplet impinging on heterogeneous substrate has a variety of potential applications. For example smart surfaces with artificially designed wettability, spatially controlled fluidic transport in microfluidic and lab-on-a chip devices and engines with internal combustion use dynamic wetting properties, see [1] for an overview. In these applications, the droplet has to be confined within a specified area and the interaction with the adjacent droplets has to be avoided when the deposited droplets are in close proximity to each other. To confine the spreading of an impinging droplet within a specified area, chemical surface coating with a pattern of high wettability contrast is often used in industrial applications. In addition, the temperature (also the magnetic or the electric) field can also be used to enhance the control on the dynamics of the droplet [1].

A number of experiments and numerical simulations have been reported in the literature for the equilibrium shape of the droplet on heterogeneous surfaces, see the recent review [1] and the references therein. Most of the numerical simulations have been performed to identify the equilibrium shape of the droplet on a

---

* Corresponding author.

E-mail addresses: sashi@serc.iisc.in (S. Ganesan), jagan@nmsc.serc.iisc.ernet.in (J. Venkatesan), sangeetha@nmsc.serc.iisc.ernet.in (S. Rajasekaran).

http://dx.doi.org/10.1016/j.ijheatmasstransfer.2015.04.043
0017-9310/

Nomenclature

α_F	convection heat transfer coefficient on liquid–gas interface
β_ϵ	slip number
Γ_F	free surface
Γ_N	non-wetting part of the solid phase
Γ_S	liquid–solid interface
γ_{ref}	reference surface tension
$\hat{\gamma}$	surface tension factor
ζ	contact line
θ_c	dynamic contact angle
θ_e^{in}	equilibrium contact angle of inner surface
θ_e^{out}	equilibrium contact angle of outer surface
λ_F	thermal conductivity of fluid
λ_S	thermal conductivity of solid
μ	dynamic viscosity of fluid
ν_F	unit outward normal vector on free surface
ν_S	unit outward normal vector on liquid-solid interface
$\boldsymbol{\nu}_\zeta$	co–normal vector at the contact line
ρ	density of fluid
ρ_S	density of solid
τ_F	unit tangential vector on free surface
τ_S	unit tangential vector on liquid–solid interface
Ω	computational domain for energy equation
Ω_F	fluid domain
Ω_S	solid domain
$\hat{\Omega}$	reference domain of ALE mapping
$\mathbb{D}$	deformation tensor of fluid velocity
$\mathbb{I}$	identity tensor
$\mathbb{S}$	stress tensor of fluid
∇_Γ	tangential gradient operator on the free surface
$\otimes$	tensor product
id_Γ	identity mapping
$\mathcal{A}_t$	ALE mapping
$\mathcal{C}_1$	negative rate of change of surface tension with temperature
tr	trace
Bi	Biot number
Fr	Froude number
Pe_F	fluid Peclet number
Pe_S	solid Peclet number
Re	reynolds number
We	weber number
c_p^F	specific heat of fluid
c_p^S	specific heat of solid
D_p^{in}	pattern diameter of the inner surface
T_∞	temperature in surrounding gas
T_F	temperature in fluid
T_{ref}	reference temperature
T_S	temperature in solid
d_0	initial droplet diameter
d/d_0	dimensionless wetting diameter
u_{imp}	impact speed
g	gravitational constant
p	pressure
q	test function in pressure space
t	time
I	end time
L	characteristic length
Q	pressure space
U	characteristic velocity
V	velocity space
$\mathbf{e}$	unit vector in the direction opposite to gravitational force
$\boldsymbol{n}$	unit outward normal on non-wetting part of solid phase
$\mathbf{u}$	fluid velocity
$\mathbf{v}$	test function in velocity space
$\mathbf{w}$	domain velocity
$\mathbf{X}$	Eulerian coordinate
$\mathbf{Y}$	ALE coordinate

heterogeneous wetting surface by minimizing the free energy with the volume constraint. The equilibrium shape of a three-dimensional (3D) droplet has been computed in [2] using the public-domain software "Surface-Evolver". The authors varied the contact angle in the free energy minimization calculation to incorporate the heterogeneous wettability effect and studied the contact angle hysteresis through the displacement of the contact line by increasing the volume of the droplet. However, the gravitational effect has not been considered in [2]. A similar approach by varying the contact angle through a position dependent interfacial energy model with gravitational effect has been presented in [3]. In particular, the authors extended the earlier model to treat chemically heterogeneous substrates with "mesa" defects. Another numerical study on the contact angle hysteresis using the free energy minimization algorithm has been presented in [4]. Recently, an analytic expression for the equilibrium droplet aspect ratio on a heterogeneous surface has been proposed in [5]. Further, the authors compared the analytically obtained aspect ratio with the numerical solution obtained using the public software "Surface-Evolver". A free energy lattice Boltzmann algorithm has also been proposed in [6] to study the droplet dynamics on chemically patterned surfaces. The authors applied a constant force (Poiseuille flow field) over the droplet to displace it on a heterogeneous surface, and studied the effect of wettability contrast. Molecular dynamics simulations for water droplets with radius of few Angstrom have been presented in [7] to study the wetting effects on a planar surface with heterogeneous wettability and on surfaces with pillars. Recently, phase-field simulations for micro-sized isothermal droplet impinging on a heterogeneous wettability surface have been presented in [8]. Even though many numerical simulations using free energy minimization algorithms have been performed for the equilibrium shape of the droplet, the flow dynamics of impinging droplets on surfaces with heterogeneous wettability has been considered only in [8].

A considerable number of numerical simulations of droplet impinging on heated solid substrates with homogeneous wettability have been reported in the literature [9–17]. The above list of references may not be complete, but to the best of the authors knowledge, simulation of droplet impinging on heated solid substrates with heterogeneous wettability has not been reported in the previous studies.

In the present study, numerical simulations of non-isothermal droplet impinging and spreading on a heated solid substrate with circular patterned heterogeneous wettability are presented. The ALE finite element scheme proposed in [17] is extended for solid substrates with heterogeneous wettability. Moreover, the Marangoni convection is included in the variational form of the Navier–Stokes equations without calculating the tangential derivative of the surface tension. In the ALE approach, the moving boundaries are resolved by moving meshes and thus the boundaries are tracked explicitly. Further, the jumps in the material coefficients and the surface force including the Marangoni effect are incorporated into the model very accurately. In addition, the energy equations in both the liquid and the solid phases are reformulated into a one-field formulation, which enables to treat the heat transfer between the phases implicitly.

2. Mathematical model

2.1. Governing equations

A liquid droplet impinging on a heated solid substrate, which contains two regions with different wetting properties is considered. The schematic representation of the considered model is shown in Fig. 1. Ω_F and Ω_S represent the fluid and solid domains, Γ_S and Γ_F represent the liquid–solid and the liquid–gas (free surface) interfaces, respectively and $\Gamma_N := \partial\Omega_S \setminus \Gamma_S$ is the non-wetting part of the solid. Further, θ_e^{in} and θ_e^{out} denote the inner and outer surface equilibrium contact angle, respectively and D_p^{in} is the inner surface pattern diameter.

We assume that the liquid is incompressible and the material properties (density, viscosity, thermal conductivity and specific heat) are constants in the liquid and in the solid phases, respectively. Detailed description of the mathematical model and the numerical scheme used in this paper has been presented in [17], whereas a brief description of the model and the numerical scheme is presented here. Let

$$x = \frac{\tilde{x}}{L}, \quad \mathbf{u} = \frac{\tilde{\mathbf{u}}}{U}, \quad \mathbf{w} = \frac{\tilde{\mathbf{w}}}{U}, \quad t = \frac{\tilde{t}U}{L},$$
$$\mathrm{I} = \frac{\tilde{\mathrm{I}}U}{L}, \quad p = \frac{\tilde{p}}{\rho U^2}, \quad \mathrm{T} = \frac{\tilde{\mathrm{T}} - \mathrm{T}_\infty}{\mathrm{T}_{ref} - \mathrm{T}_\infty}$$

be the dimensionless length, fluid velocity, domain velocity, time, given end time, pressure and temperature, respectively, whereas the tilde denotes the respective dimensional quantities. Here, L and U are characteristic length and velocity scales, ρ denotes the density of the fluid, T_∞ denotes the temperature in the surrounding gas and T_{ref} is a given reference temperature at which the surface tension is γ_{ref}. Further, we define the dimensionless numbers (Reynolds, Weber, Froude and slip, respectively) as

$$\mathrm{Re} = \frac{\rho U L}{\mu}, \quad \mathrm{We} = \frac{\rho U^2 L}{\gamma_{ref}}, \quad \mathrm{Fr} = \frac{U^2}{Lg}, \quad \beta_\epsilon = \frac{1}{\epsilon_\mu \rho U},$$

where g is the gravitational constant, ϵ_μ is the slip coefficient in the Navier–slip with friction boundary condition. Given these numbers, the fluid flow in the droplet is described by the time-dependent incompressible Navier–Stokes equations

$$\frac{\partial \mathbf{u}}{\partial t} + (\mathbf{u}\cdot\nabla)\mathbf{u} - \nabla\cdot\mathbb{S}(\mathbf{u},p) = \frac{1}{\mathrm{Fr}}\mathbf{e} \quad \text{in } \Omega_F(t)\times(0,\mathrm{I}), \tag{1}$$
$$\nabla\cdot\mathbf{u} = 0 \quad \text{in } \Omega_F(t)\times(0,\mathrm{I}) \tag{2}$$

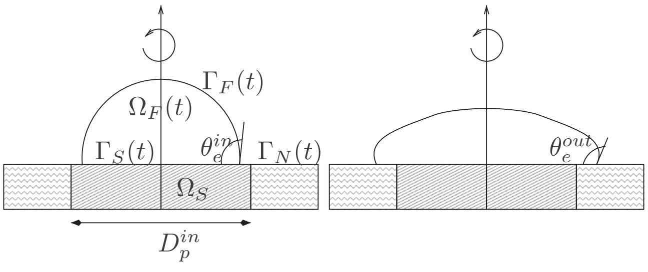

Fig. 1. Computational model of an impinging droplet on a hot solid substrate, which contains inner and outer regions with different wetting properties.

with the initial condition

$$\mathbf{u}(\cdot,0) = \mathbf{u}_0/U,$$

the force balance (neglecting the dilatational surface viscosity and the surface shear viscosity in the Boussinesq–Scriven law) and the kinematic condition

$$\mathbb{S}(u,p)\cdot\boldsymbol{\nu}_F = \frac{1}{\mathrm{We}}\nabla_\Gamma\cdot(\hat{\gamma}\nabla_\Gamma id_\Gamma), \quad \mathbf{u}\cdot\boldsymbol{\nu}_F = \mathbf{w}\cdot\boldsymbol{\nu}_F$$

on the free surface $\Gamma_F(t)$, and the Navier–slip boundary condition

$$\mathbf{u}\cdot\boldsymbol{\nu}_S = 0, \quad \boldsymbol{\tau}_{i,S}\cdot\mathbb{S}(\mathbf{u},p)\cdot\boldsymbol{\nu}_S = -\beta_\epsilon(\mathbf{u}\cdot\boldsymbol{\tau}_{i,S})$$

on the liquid–solid interface $\Gamma_S(t)$. Here, $\mathbf{e}$ is the unit vector in the direction opposite to the gravitational force. The dimensionless stress tensor $\mathbb{S}(\mathbf{u},p)$ and the deformation tensor $\mathbb{D}(\mathbf{u})$ for the incompressible Newtonian fluid are given by

$$\mathbb{S}(\mathbf{u},p) = \frac{2}{\mathrm{Re}}\mathbb{D}(\mathbf{u}) - p\mathbb{I}, \quad \mathbb{D}(\mathbf{u}) = \frac{1}{2}\left(\nabla\mathbf{u} + \nabla\mathbf{u}^{\mathrm{T}}\right).$$

Here, $\mathbb{I}$ is the identity tensor. Further, $\mathbf{u}_0 = (0,0,-u_{imp})$ is the initial velocity with the impact speed u_{imp}, id_Γ is an identity mapping and ∇_Γ is the tangential gradient operator on the free surface. For instance, the tangential gradient of the scalar field ϕ and the tangential divergence of a vector field $\mathbf{v}$ are defined by

$$\nabla_\Gamma\phi = (\mathbb{I} - \boldsymbol{\nu}_F\otimes\boldsymbol{\nu}_F)\phi, \quad \nabla_\Gamma\cdot\mathbf{v} = \mathrm{tr}(\nabla_\Gamma\mathbf{v}).$$

Note that the restriction of $\nabla_\Gamma\phi$ onto $\Gamma_F(t)$ depends only on the values of ϕ on $\Gamma_F(t)$. The temperature-dependent surface tension factor is given by

$$\hat{\gamma}(\mathrm{T}_F) = 1 - \frac{\mathcal{C}_1}{\gamma_{ref}}(\mathrm{T}_F - 1). \tag{3}$$

Here, T_F is the dimensionless temperature on the free surface and $\mathcal{C}_1 > 0$ is the negative rate of change of surface tension with temperature. In computations, $\mathcal{C}_1/\gamma_{ref} = 0.002$ is used.

Next, the distribution of the temperature in the liquid droplet and in the solid substrate is described by the dimensionless energy equations

$$\frac{\partial \mathrm{T}_F}{\partial t} + \mathbf{u}\cdot\nabla\mathrm{T}_F - \frac{1}{\mathrm{Pe}_F}\Delta\mathrm{T}_F = 0 \quad \text{in } \Omega_F(t)\times(0,\mathrm{I}), \tag{4}$$

$$\frac{\partial \mathrm{T}_S}{\partial t} - \frac{1}{\mathrm{Pe}_S}\Delta\mathrm{T}_S = 0 \quad \text{in } \Omega_S(t)\times(0,\mathrm{I}) \tag{5}$$

with the initial conditions

$$\mathrm{T}_F(x,0) = \frac{\mathrm{T}_F(0) - \mathrm{T}_\infty}{\mathrm{T}_{ref} - \mathrm{T}_\infty} \quad \text{in } \Omega_F(0),$$

$$\mathrm{T}_S(x,0) = \frac{\mathrm{T}_S(0) - \mathrm{T}_\infty}{\mathrm{T}_{ref} - \mathrm{T}_\infty} \quad \text{in } \Omega_S(0)$$

and boundary conditions

$$\begin{aligned} -\frac{\partial \mathrm{T}_F}{\partial \boldsymbol{\nu}_F} &= \mathrm{Bi}\mathrm{T}_F \quad \text{on } \Gamma_F(t)\times(0,\mathrm{I}),\\ \mathrm{T}_F = \mathrm{T}_S, \quad \frac{\partial \mathrm{T}_F}{\partial \boldsymbol{\nu}_F} &= -\frac{\lambda_S}{\lambda_F}\frac{\partial \mathrm{T}_S}{\partial \boldsymbol{\nu}_S} \quad \text{on } \Gamma_S(t)\times(0,\mathrm{I}),\\ \frac{\partial \mathrm{T}_S}{\partial \boldsymbol{n}} &= 0 \quad \text{on } \Gamma_N(t)\times(0,\mathrm{I}). \end{aligned} \tag{6}$$

Here, $\mathrm{T}_F(0)$ and $\mathrm{T}_S(0)$ denote the initial temperature in the fluid and solid phases, respectively, and the dimensionless (Peclet and the Biot) numbers are given by

$$\mathrm{Pe}_F = \frac{LUc_p^F\rho}{\lambda_F}, \quad \mathrm{Pe}_S = \frac{LUc_p^S\rho_S}{\lambda_S}, \quad \mathrm{Bi} = \frac{\alpha_F L}{\lambda_F},$$

where $\lambda_F,\ \lambda_S$ the thermal conductivities, $\rho,\ \rho_S$ the densities, $c_p^F,\ c_p^S$ the specific heat of the fluid and the solid phases. Further, α_F is the convection heat transfer coefficient on the liquid–gas interface and $\boldsymbol{n}$ is the unit outward normal on Γ_N.

3. Numerical scheme

3.1. ALE approach for time-dependent domains

The free surface of the droplet is tracked by the ALE approach using moving meshes, which resolve interfaces and boundaries. Since the liquid–solid interface is resolved by the moving mesh in $\Omega_F(t)$, the solid substrate Ω_S also become time-dependent. Therefore, the energy equations in both the liquid and solid phases have to be reformulated to an ALE form, in addition to the derivation of the Navier–Stokes equations.

Let $\Omega(t) := \Omega_F(t) \cup \Omega_S \cup \Gamma_S(t)$ be the domain for the energy equation, and $\hat\Omega$ (often the previous time step domain in computations) be its reference domain. Define a family of ALE mapping

$$\mathcal{A}_t : \hat\Omega \to \Omega(t), \quad \mathcal{A}_t(\mathbf{Y}) = \mathbf{X}(\mathbf{Y}, t), \quad t \in (0, \mathrm{I}).$$

Assume that the mapping $\mathcal{A}_t$ for all $t \in (0, \mathrm{I})$ is homeomorphic, that is, $\mathcal{A}_t$ is bijective, continuous and its inverse $\mathcal{A}_t^{-1}$ is also continuous. Further, assume that the mappings are differentiable almost everywhere in $(0, \mathrm{I})$. We call $\mathbf{Y}$ as the ALE coordinate while $\mathbf{X}$ as the Eulerian coordinate. For a scalar function $v : \Omega(t) \times (0, \mathrm{I}) \to \mathbb{R}$, which is defined on the Eulerian frame, define their corresponding $\hat v$ on the ALE frame as

$$\hat v : \hat\Omega \times (0, \mathrm{I}) \to \mathbb{R}, \quad (\mathbf{Y}, t) \mapsto v(\mathbf{X}(\mathbf{Y}, t), t) = v(\mathcal{A}_t(\mathbf{Y}), t).$$

Further, the time derivative of v on the ALE frame is given by

$$\left.\frac{\partial v}{\partial t}\right|_{\hat\Omega} : \Omega(t) \times (0, \mathrm{I}) \to \mathbb{R}, \quad (\mathbf{X}, t) \mapsto \frac{\partial \hat v}{\partial t}(\mathcal{A}_t^{-1}(\mathbf{X}), t)$$

and the domain velocity on the ALE frame is defined by

$$\mathbf{w}(\mathbf{X}, t) = \left.\frac{\partial \mathbf{X}}{\partial t}\right|_{\hat\Omega}(\mathcal{A}_t^{-1}(\mathbf{X}), t), \quad \mathbf{X} \in \Omega(t).$$

In order to write the model equations in the ALE frame, apply the chain rule to the time derivative of v in the ALE frame to get

$$\left.\frac{\partial v}{\partial t}\right|_{\hat\Omega} = \frac{\partial v}{\partial t} + \frac{\partial v}{\partial \mathbf{X}}\left.\frac{\partial \mathbf{X}}{\partial t}\right|_{\hat\Omega}(\mathcal{A}_t^{-1}(\mathbf{X}), t) = \frac{\partial v}{\partial t} + \mathbf{w} \cdot \nabla v. \tag{7}$$

Using (7) we now transform the time derivatives in the model equations into the ALE frame and obtain

$$\left.\frac{\partial \mathbf{u}}{\partial t}\right|_{\hat\Omega} + ((\mathbf{u} - \mathbf{w}_F) \cdot \nabla)\mathbf{u} - \nabla \cdot \mathbb{S}(\mathbf{u}, p) = \frac{1}{\mathrm{Fr}}\mathbf{e}, \tag{8}$$

$$\left.\frac{\partial \mathrm{T}_F}{\partial t}\right|_{\hat\Omega} + (\mathbf{u} - \mathbf{w}_F) \cdot \nabla \mathrm{T}_F - \frac{1}{\mathrm{Pe}_F}\Delta \mathrm{T}_F = 0, \tag{9}$$

$$\left.\frac{\partial \mathrm{T}_S}{\partial t}\right|_{\hat\Omega} - \mathbf{w}_S \cdot \nabla \mathrm{T}_S - \frac{1}{\mathrm{Pe}_S}\Delta \mathrm{T}_S = 0, \tag{10}$$

where $\mathbf{w}_F = \mathbf{w}|_{\Omega_F}$ and $\mathbf{w}_S = \mathbf{w}|_{\Omega_S}$.

3.2. Variational form

The variational form of the Navier–Stokes equations and the energy equations are derived in the usual way. Let L^2, H^1 and $(\cdot,\cdot)_\Omega$ be the Sobolev spaces and the inner product in $L^2(\Omega)$ and its vector-valued versions. We now define the velocity and pressure spaces as

$$V := \left\{\mathbf{v} \in H^1(\Omega_F(t))^3 : \mathbf{v} \cdot \boldsymbol{\nu}_S = 0 \text{ on } \Gamma_S(t)\right\}, \quad Q := L^2(\Omega_F(t)),$$

where the no penetration boundary condition $\mathbf{u} \cdot \boldsymbol{\nu}_S = 0$ on liquid–solid interface $\Gamma_S(t)$ is incorporated in the velocity space. Next, multiply the ALE form of the momentum conservation equation (8) and the mass balance equation (2) by test functions $\mathbf{v} \in V$ and $q \in Q$ respectively, and integrate over $\Omega_F(t)$. Applying the Gaussian theorem to the stress tensor, we get

$$-\int_{\Omega_F(t)} \nabla \cdot \mathbb{S}(\mathbf{u}, p) \cdot \mathbf{v}\, dx + \int_{\partial\Omega_F(t)} \mathbf{v} \cdot \mathbb{S}(\mathbf{u}, p) \cdot \boldsymbol{\nu}\, d\gamma = \frac{2}{\mathrm{Re}}\int_{\Omega_F(t)} \mathbb{D}(\mathbf{u}) : \mathbb{D}(\mathbf{v})\, dx - \int_{\Omega_F(t)} p \nabla \cdot \mathbf{v}\, dx.$$

We now split the boundary integral as

$$\int_{\partial\Omega_F(t)} \mathbf{v} \cdot \mathbb{S}(\mathbf{u}, p) \cdot \boldsymbol{\nu}\, d\gamma = \int_{\Gamma_S(t)} \mathbf{v} \cdot \mathbb{S}(\mathbf{u}, p) \cdot \boldsymbol{\nu}_S\, d\gamma_S + \int_{\Gamma_F(t)} \mathbf{v} \cdot \mathbb{S}(\mathbf{u}, p) \cdot \boldsymbol{\nu}_F\, d\gamma_F.$$

Using the orthonormal decomposition

$$\mathbf{v} = (\mathbf{v} \cdot \boldsymbol{\nu}_S)\boldsymbol{\nu}_S + \sum_{i=1}^{2}(\mathbf{v} \cdot \boldsymbol{\tau}_{i,S})\boldsymbol{\tau}_{i,S} \quad \text{on } \Gamma_S,$$

the integral over $\Gamma_S(t)$ becomes

$$\int_{\Gamma_S(t)} \mathbf{v} \cdot \mathbb{S}(\mathbf{u}, p) \cdot \boldsymbol{\nu}_S\, d\gamma_S = -\beta_\epsilon \sum_{i=1}^{2}\int_{\Gamma_S(t)} (\mathbf{u} \cdot \boldsymbol{\tau}_{i,S})(\mathbf{v} \cdot \boldsymbol{\tau}_{i,S})\, d\gamma_S.$$

Note that this integral term will be on the left hand side of the system, and it adds stability to the system. We next include the force balancing condition on the free surface with Marangoni effects into the variational form without evaluating the tangential gradient of the surface tension. This approach is different from our earlier approach, where the Laplace–Beltrami operator has been used to handle the curvature [17–19]. After incorporating the force balancing condition, the integral over free surface becomes

$$\begin{aligned}
-\int_{\Gamma_F(t)} \mathbf{v} \cdot \mathbb{S}(\mathbf{u}, p) \cdot \boldsymbol{\nu}_F\, d\gamma_F &= -\frac{1}{\mathrm{We}}\int_{\Gamma_F(t)} \mathbf{v} \cdot \nabla_\Gamma \cdot (\hat\gamma \nabla_\Gamma id_\Gamma)\, d\gamma_F \\
&= \frac{1}{\mathrm{We}}\int_{\Gamma_F(t)} \hat\gamma \nabla_\Gamma id_\Gamma : \nabla_\Gamma \mathbf{v}\, d\gamma_F \\
&\quad - \frac{1}{\mathrm{We}}\int_{\zeta(t)} \hat\gamma \boldsymbol{\nu}_\zeta \cdot \mathbf{v}\, d\zeta,
\end{aligned}$$

where $\zeta(t)$ is the contact line and $\boldsymbol{\nu}_\zeta$ is the co-normal vector at the contact line, which is normal to ζ and tangent to $\Gamma_F(t)$. After including the contact angle in the integral over the contact line, as in [17], the variational form of the Navier–Stokes equations read.

For given $\mathbf{u}_0$ and $\Omega_F(0)$, find $(\mathbf{u}, p) \in V \times Q$ such that

$$\left(\frac{\partial \mathbf{u}}{\partial t}, \mathbf{v}\right)_{\hat\Omega_F} + a(\mathbf{u} - \mathbf{w}; \mathbf{u}, \mathbf{v}) - b(p, \mathbf{v}) + b(q, \mathbf{u}) = f(\mathbf{v}) \tag{11}$$

for all $(\mathbf{v}, q) \in V \times Q$, where

$$a(\hat{\mathbf{u}}; \mathbf{u}, \mathbf{v}) = \frac{2}{\mathrm{Re}}\int_{\Omega_F(t)} \mathbb{D}(\mathbf{u}) : \mathbb{D}(\mathbf{v}) + (\hat{\mathbf{u}} \cdot \nabla)\mathbf{u} \cdot \mathbf{v}\, dx + \beta_\epsilon \int_{\Gamma_S(t)} \sum_{i=1}^{2}(\mathbf{u} \cdot \boldsymbol{\tau}_{i,S})(\mathbf{v} \cdot \boldsymbol{\tau}_{i,S})\, d\gamma_S,$$

$$b(q, \mathbf{v}) = \int_{\Omega_F(t)} q \nabla \cdot \mathbf{v}\, dx,$$

$$f(\mathbf{v}) = \frac{1}{\mathrm{Fr}}\int_{\Omega_F(t)} \mathbf{e} \cdot \mathbf{v}\, dx - \frac{1}{\mathrm{We}}\int_{\Gamma_F(t)} \hat\gamma \nabla_\Gamma id_\Gamma : \nabla_\Gamma \mathbf{v}\, d\gamma_F + \frac{1}{\mathrm{We}}\int_{\zeta(t)} \hat\gamma \cos(\theta(\zeta))\, \mathbf{v} \cdot \boldsymbol{\tau}_S\, d\zeta.$$

Here, the space-dependent contact angle is defined as

$$\theta(\zeta) = \begin{cases} \theta_e^{in} & \text{if} \quad \zeta \leqslant D_p^{in} - 0.01 \\ c\theta_e^{in} + (1-c)\theta_e^{out} & \text{if} \quad D_p^{in} - 0.01 < \zeta < D_p^{in} + 0.01 \\ \theta_e^{out} & \text{if} \quad \zeta \geqslant D_p^{in} + 0.01, \end{cases}$$

where $c = \left(0.01 + D_p^{in} - \zeta\right)/0.02$.

Remark. Note that the Marangoni convection is included in the variational form (11) without calculating the tangential derivative of the surface tension. Consequently, the partial derivatives of the temperature are no longer needed to incorporate the Marangoni effects, and thus, a piecewise constant or a piecewise linear finite elements can also be used for the finite element approximation of the temperature. Further, the contact angle in the source term $f(\mathbf{v})$ is now position dependent and it includes the heterogeneous wettability into the model.

We next derive the variational form of the energy equation in the liquid and in the solid substrate as a single equation in $\Omega(t)$. We first multiply the Eq. (9) with a test function $\psi_F \in H^1(\Omega_F)$, apply integration by parts and incorporate boundary conditions to get

$$\int_{\Omega_F(t)} \frac{\partial \mathrm{T}_F}{\partial t}\psi_F dx + \int_{\Omega_F(t)} ((\mathbf{u} - \mathbf{w}_F)\cdot\nabla)\mathrm{T}_F\psi_F dx + \frac{1}{\mathrm{Pe}_F}\int_{\Omega_F(t)} \nabla\mathrm{T}_F\cdot\nabla\psi_F dx$$
$$+ \int_{\Gamma_F(t)} \frac{\mathrm{Bi}}{\mathrm{Pe}_F}\mathrm{T}_F\psi_F d\gamma_F = -\frac{1}{\mathrm{Pe}_F}\frac{\lambda_S}{\lambda_F}\int_{\Gamma_S(t)} \frac{\partial \mathrm{T}_S}{\partial \boldsymbol{v}_S}\psi_F d\gamma_F. \qquad (12)$$

Similarly, multiplying (10) with a test function $\psi_S \in H^1(\Omega_S)$, and after applying integration by parts and incorporating boundary conditions, we obtain

$$\int_{\Omega_S(t)} \frac{\partial \mathrm{T}_S}{\partial t}\psi_S dx + \int_{\Omega_S(t)} (\mathbf{w}_S\cdot\nabla)\mathrm{T}_S\psi_S dx + \frac{1}{\mathrm{Pe}_S}\int_{\Omega_S(t)} \nabla\mathrm{T}_S\cdot\nabla\psi_S dx$$
$$= \frac{1}{\mathrm{Pe}_S}\int_{\Gamma_S(t)} \frac{\partial \mathrm{T}_S}{\partial \boldsymbol{v}_S}\psi_S d\gamma_S. \qquad (13)$$

Using

$$\mathbf{u}_T(x,t) = \begin{cases} \mathbf{u}(x,t) & \text{if} \quad x \in \Omega_F(t), \\ 0 & \text{if} \quad x \in \Omega_S, \end{cases}$$

$$\mathrm{T}(x,t) = \begin{cases} \mathrm{T}_F(x,t) & \text{if} \quad x \in \Omega_F(t), \\ \mathrm{T}_S(x,t) & \text{if} \quad x \in \Omega_S, \end{cases}$$

$$\mathrm{Pe}(x) = \begin{cases} \mathrm{Pe}_F & \text{if} \quad x \in \Omega_F(t), \\ \frac{\lambda_F}{\lambda_S}\mathrm{Pe}_F & \text{if} \quad x \in \Omega_S, \end{cases}$$

$$g(x) = \begin{cases} 1 & \text{if} \quad x \in \Omega_F(t), \\ \frac{\lambda_S \mathrm{Pe}_S}{\lambda_F \mathrm{Pe}_F} & \text{if} \quad x \in \Omega_S. \end{cases}$$

$$\mathrm{T}_0(x) = \begin{cases} \mathrm{T}_F(x,0) & \text{if} \quad x \in \Omega_F(0), \\ \mathrm{T}_S(x,0) & \text{if} \quad x \in \Omega_S, \end{cases}$$

the one-field variational form of the energy equation is obtain as:

For given $\Omega(0)$, $\mathbf{u}_T$, $\mathbf{w}$ and T_0, find $\mathrm{T} \in H^1(\Omega(t))$ such that

$$\left(g\frac{\partial \mathrm{T}}{\partial t}, \psi\right)_\Omega + a_T(\mathbf{u}_T - \mathbf{w}; \mathrm{T}, \psi) + b_T(\mathrm{T}, \psi) = 0 \qquad (14)$$

for all $\psi \in H^1(\Omega(t))$, where

$$a_T(\mathbf{u}; \mathrm{T}, \psi) = \int_{\Omega(t)} \frac{1}{\mathrm{Pe}}\nabla\mathrm{T}\cdot\nabla\psi dx + \int_{\Omega(t)} (\mathbf{u}\cdot\nabla)\mathrm{T}\psi dx,$$

$$b_T(\mathrm{T}, \psi) = \mathrm{Bi}\int_{\Gamma_F(t)} \frac{1}{\mathrm{Pe}}\mathrm{T}\psi dx.$$

3.3. Spatial and temporal discretization

Let $0 = t^0 < t^1 < \cdots < t^N = \mathrm{I}$ be a decomposition of the time interval $[0, \mathrm{I}]$, and $\delta t = t^n - t^{n-1}$ be an uniform time step. We then apply the fractional-step-θ scheme, which – on fixed domains – is strongly A-stable and of second-order convergent [20, Chapter 3.2.1], to the time derivatives in the variational forms (11) and (14) to obtain the temporal discretization.

Using the axisymmetric assumption, we next obtain the 3D-axisymmetric weak form in a 2D-meridian domain from (11) and (14) by transforming the volume, surface and line integrals into the area, line and a functional in the contact point as described in [21] for interface flows. The axisymmetric formulation reduces the computational cost drastically, and allows to use 2D finite elements for spatial discretization.

In the ALE approach, the free surface is resolved by the computational mesh. Further, the kinematic condition

$$\mathbf{u}\cdot\boldsymbol{v}_F = \mathbf{w}\cdot\boldsymbol{v}_F$$

has to be satisfied on the free surface while moving the free surface. Thus, an accurate velocity approximation, at least of second-order, is preferred. Therefore, we use the inf-sup stable finite-element pair (P_2, P_1), i.e., continuous, piecewise quadratic polynomials for the velocity components and continuous, piecewise linear polynomials for the pressure [22]. For the spatial discretization of the energy equation a continuous, piecewise quadratic finite elements is used.

3.4. Free surface tracking and mesh update

To realize the ALE implementation, we first calculate the mesh velocity at each time step. The computation of the fluid mesh velocity $\mathbf{w}_F$ is presented here, whereas the solid phase mesh velocity is obtained in a similar way. At time $t = t^n$, let Ψ_F^n be the displacement vector in $\widehat{\Omega}_F$, and $\mathbf{X}^n$ be the new position for all $\mathbf{X}^{n-1} \in \partial\Omega_F(t^{n-1})$, for example, at the beginning $n = 1$, we start with $\mathbf{X}^1 = \mathbf{X}^0 + \delta t\mathbf{u}_0$. We then obtain the displacement of the inner points by solving the linear elasticity equation with Dirichlet boundary condition

$$\begin{aligned} \nabla\cdot\mathbb{T}(\Psi^n) &= 0 \quad \text{in } \widehat{\Omega_F}(t_n) \\ \Psi^n &= \mathbf{X}^n - \mathbf{X}^{n-1} \quad \text{on } \partial\widehat{\Omega_F}(t_n), \end{aligned} \qquad (15)$$

where $\mathbb{T}(\phi) = \lambda_1(\nabla\cdot\phi)\mathbb{I} + 2\lambda_2\mathbb{D}(\phi)$. Here, λ_1 and λ_2 are Lame constants, and in computations we used $\lambda_1 = \lambda_2 = 1$. Once the displacement vector is calculated, the mesh velocity is then calculated as $\mathbf{w}^n = \Psi^n/\delta t$. After that we solve the discrete form of the Navier–Stokes equation (11) by considering the temperature explicitly. In the solution of the Navier–Stokes equations, a fixed point iteration, as in [21], is used to handle the nonlinear convection term, that is, at time t^n, starting with $\mathbf{u}_0^n := \mathbf{u}^{n-1}$, $\mathbf{w}_0^n := \mathbf{w}^{n-1}$ and replacing the form $a(\mathbf{u}^n - \mathbf{w}^n, \mathbf{u}^n, \mathbf{v})$ by $a(\mathbf{u}_{i-1}^n - \mathbf{w}_{i-1}^n, \mathbf{u}_i^n, \mathbf{v})$, $i = 1, 2, \ldots$, and iterate (solve the linear system) until the residual of the Navier–Stokes equations reduces to 10^{-8}. Note that in each step of the fixed point iteration, the linear elasticity problem (15) has to be solved, 'virtually' without moving the mesh, in order to treat the mesh velocity $\mathbf{w}^n$ implicit. Further, the free surface force term in $f(\mathbf{v})$ is treated semi-implicitly as in [17].

We then calculate the mesh velocity $\mathbf{w}_S^n$, in a similar way, and solve the discrete form of the energy equation (14) with the updated flow velocity and the mesh velocity. Finally, we move the mesh with the computed displacement and advance to the next time step.

During the mesh movement, the free surface adjacent to the contact line may reach the solid surface due to rolling motion of the droplet. Since the boundary resolved mesh is used in the ALE approach, the rolling motion leads to a non-matching grid along the liquid–solid interface. Therefore, a mesh manipulation technique which maintains a matching grid when a free surface vertex reaches the solid surface is implemented, see [17] for a detailed description. Further, an automatic remeshing algorithm is used to remesh the domain when the quality of the mesh become very poor, say if the minimum angle becomes less than 10°.

4. Numerical results

In this section, we present a detailed numerical investigation on the impingement and spreading of a 3D-axisymmetric non-isothermal liquid droplet on a heated solid substrate with heterogeneous wettability. We first perform a mesh convergence study for a non-isothermal droplet impinging on a homogeneous solid substrate. We then validate the numerical scheme for an isothermal liquid droplet impinging on a homogeneous solid substrate using the experimental data presented in [15]. The proposed numerical scheme guarantees the conservation of mass and energy well, and it is demonstrated by calculating the relative mass and internal energy fluctuations. We then consider a non-isothermal droplet impingement on a solid substrate with circular patterned heterogeneous wettability, see Fig. 1. The effects of wettability contrast, pattern diameter, Reynolds number and Weber number on the confinement of the droplet spreading are studied. Further, the influence of these parameters on the total heat transfer from the solid substrate to the liquid droplet is examined. The total heat

$$\int_0^t \int_{\Gamma_S(t)} \frac{1}{\mathrm{Pe}_S} \frac{\partial \mathrm{T}_S}{\partial \boldsymbol{\nu}_S} d\gamma_S$$

is calculated using the variational form, and we refer to [17] for the detailed derivation. Unless specified, we use a constant time step $\delta t = 0.00025$ and 200 vertices on the free surface with the initial edge size $h_0 = 0.00778929$. Fig. 2 depicts an initial mesh used in computations. Further, a mesh-dependent slip number $\beta_\epsilon = 8.26/2h_0$ is used in computations unless specified, and the reader is referred to [23] for the choice of a slip number. Moreover, we limit the maximum area of each cell in the mesh to 0.00625 during the triangulation, and it results in 1364 and 2164 cells in the initial liquid and solid domains, respectively. This choice of initial mesh results in 5966 velocity, 810 pressure and 7443 temperature degrees of freedom. However, the number of cells and the degrees of freedom may vary during remeshing.

4.1. Validation

In this section, we first perform a mesh convergence study for the proposed numerical scheme. We consider a water droplet of diameter $d_0 = 5.5 \times 10^{-5}$ m impinging with an impact speed of $u_{imp} = 2.45$ m/s on a homogeneous hot solid substrate. Further, the following material parameters are used: density $\rho = 1000$ kg/m^3, surface tension $\sigma = 0.0728$ N/m, dynamic viscosity $\mu = 8.9 \times 10^{-4}$ N s/m^2, and the equilibrium contact angle $\theta_e = 50^\circ$. Also, we take $\mathrm{T}_S(0) = 328$ K, $\mathrm{T}_F(0) = 298$ K, $\mathrm{T}_\infty = 298$ K and $\mathrm{T}_{\mathrm{ref}} = 323$ K. Using the characteristic length $L = d_0$ and characteristic velocity $U = u_{imp}$, we get $\mathrm{Re} = 151$, $\mathrm{We} = 4.5$, $\mathrm{Fr} = 11,125$, $\mathrm{Pe}_S = 200$, $\mathrm{Pe}_F = 20$ and $\mathrm{Bi} = 0.000116$. To perform a mesh convergence study, we vary the number of vertices on the free surface boundary. The initial mesh (L0) consists of 25 vertices on the free surface with h_0=0.06334015 and the successive mesh levels are generated by doubling the number of vertices on the free surface and halving the cell area of the previous level mesh. Four variants with different number of vertices on the free surface are used: (i) L0 with 25 vertices (ii) L1 with 50 vertices, (iii) L2 with 100 vertices and (iv) L3 with 200 vertices. The wetting diameter and dynamic contact angle for all the mesh levels are shown in Fig. 3. From both pictures in Fig. 3, we can observe the convergence with L2 and L3 meshes.

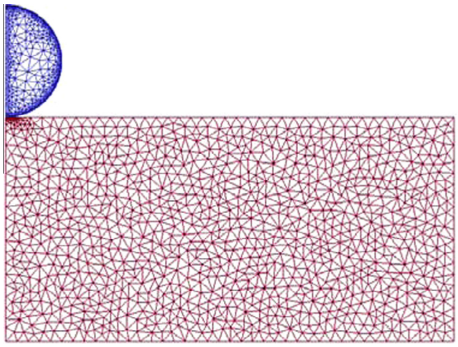

Fig. 2. Computational mesh of an impinging droplet on a hot solid substrate.

To validate the numerical scheme, we now compare the numerically obtained wetting diameter and the apex height of

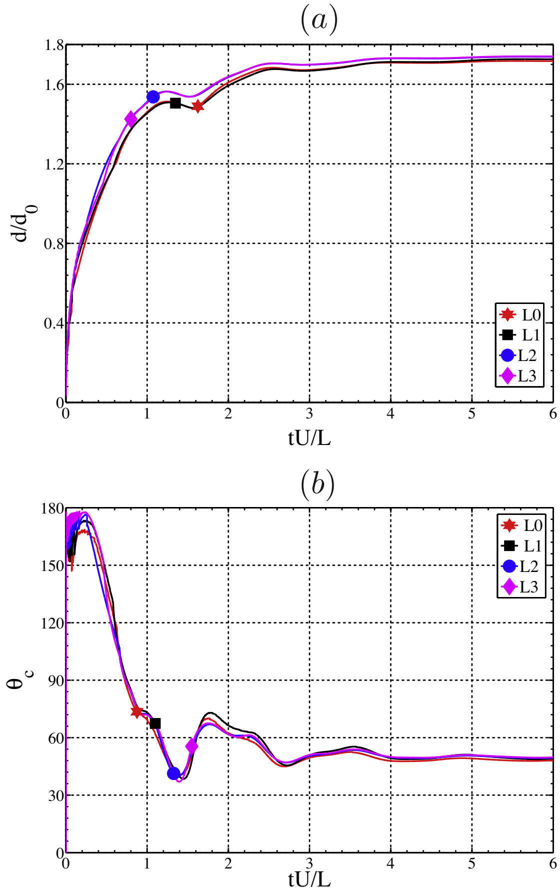

Fig. 3. Computationally obtained wetting diameter (a) and the dynamic contact angle (b) of an impinging droplet with $\theta_e = 50^\circ$, Re = 151, We = 4.5 and Fr = 11,125 for different number of vertices on the free surface boundary.

the impinging water droplet with the experimental results presented in [15]. We consider an isothermal water droplet with same material properties as in the mesh convergence study, and for the corresponding experimental data we refer to droplet C in Table 1 of [15]. The used dimensionless numbers are Re $= 151$, We $= 4.5$ and Fr = 11125. The computationally obtained wetting diameter and the apex height of the droplet are compared with the experimental results in Fig. 4. The wetting diameter curve fits very well with the experimental result, whereas the numerically obtained apex height of the droplet is less oscillatory compared to the experimental data. Due to non-symmetric capillary waves, a large oscillation in the apex height of the droplet could have been observed in experiments, whereas the axisymmetric numerical model is used here. Nevertheless, the difference is less and the behavior is similar. Moreover, the wetting diameter of the droplet is the key factor for the heat transfer and for the effect of the wettability contrast in the flow dynamics, and it fits well with experiments.

Guaranteeing the mass and the energy conservation is very crucial in computations of free surface flows, as mass loss results in completely unphysical solutions. Therefore, verifying the conservation properties is another measure to determine the accuracy of the numerical scheme. To verify the mass and the energy conservation properties, we consider a droplet of diameter $d_0 = 2.7 \times 10^{-3}$ m impinging with an impact velocity of $u_{imp} = 1.54$ m/s. Further, we assume that the product of the specific heat and density is same in both the liquid and solid phases. Computations are performed for two test cases (i) Re = 260 and (ii) Re = 2079, with We = 43, Fr = 179, $\mathrm{Pe}_F = 10$, $\mathrm{Pe}_S = 100$, Bi = 0 and $\theta_e = 30^\circ$. Further, we use $T_F(0) = 298$ K, $T_S(0) = 328$ K, $T_\infty = 298$ K and $T_{ref} = 323$ K in both the test cases. We calculate the relative mass and internal energy fluctuation using

$$\text{mass fluctuation} := \frac{\int_{\Omega_F(0)} dx - \int_{\Omega_F(t)} dx}{\int_{\Omega_F(0)} dx},$$

$$\text{internal energy fluctuation} := \frac{\int_{\Omega(0)} T\,dx - \int_{\Omega(t)} T\,dx}{\int_{\Omega(0)} T\,dx}$$

with Bi = 0. Note that, the mass of the solid substrate does not change, and thus it is enough to verify the mass fluctuation in $\Omega_F(t)$. Further, the internal energy in liquid and solid substrate must be conserved due to the choice of the adiabatic conditions on Γ_F and Γ_N in (6). The mass and the internal energy fluctuations obtained in computations of both test cases are presented in Fig. 5. Even in the high Reynolds number case, the relative mass and the internal energy fluctuations are less than 10^{-2} and 10^{-3}, respectively, and it shows the accuracy of the numerical scheme.

4.2. Effect of wettability contrast

The equilibrium contact angle depends on the surface properties of the solid substrate, and these properties can be modified selectively by chemical coating. As already mentioned in the introduction, chemical surface patterning with sufficient wettability contrast is one of the popular techniques to confine the spreading of an impinging droplet within a specified area. In order to confine the droplet within a specified area, the inner region of the circular pattern is made more wettable than the surface surrounding it, i.e., $\theta_e^{in} \leqslant \theta_e^{out}$. In this section we study the effect of wettability contrast

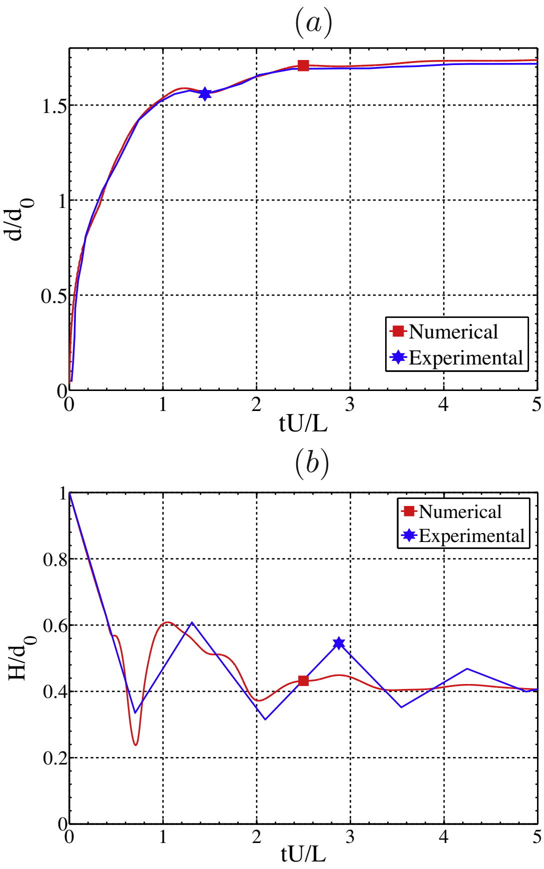

Fig. 4. Comparison of numerical simulations with experimental results. Wetting diameter (a) and the apex height (b) of the impinging droplet with $\theta_e = 50^\circ$, Re = 151, We = 4.5 and Fr = 11,125.

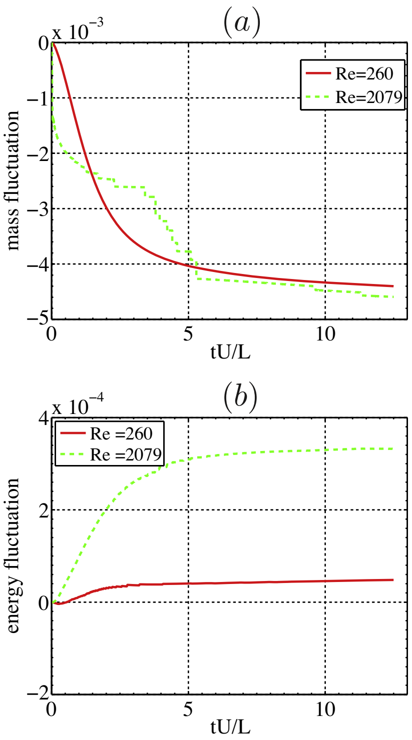

Fig. 5. The mass (a) and the internal energy (b) fluctuations in computations of impinging droplets in two test cases, (i) Re = 260 and (ii) Re = 2079, with We = 43, Fr = 179, $\mathrm{Pe}_F = 10$, $\mathrm{Pe}_S = 100$, Bi = 0 and $\theta_e = 30^\circ$.

on the spreading and confinement of a non-isothermal impinging droplet.

We consider a water droplet with the same material properties as in the mesh convergence study which result in Re = 151, We = 4.5, Fr = 11,125, $\text{Pe}_F = 20$, $\text{Pe}_S = 200$ and Bi = 0.000116. In order to study the effect of wettability contrast, a set of simulations by varying the contact angle of the outer surface: (i) $\theta_e^{out} = 50^\circ$, (ii) $\theta_e^{out} = 55^\circ$, (iii) $\theta_e^{out} = 70^\circ$, (iv) $\theta_e^{out} = 90^\circ$ and (v) $\theta_e^{out} = 120^\circ$ are performed. Further, the contact angle of the inner surface is fixed as $\theta_e^{in} = 50^\circ$. Two sets of simulations with (1) $D_p^{in} = 1.2$ and (2) $D_p^{in} = 1.4$ for the above variants are performed. The values for D_p^{in} are chosen in such a way that it is less than the final wetting diameter when the same droplet spreads on a homogeneous surface.

The numerical results of the above variants are presented in Figs. 6 and 7. We can observe that the equilibrium wetting diameter, (c) in Figs. 6 and 7, reduces significantly with increasing the wettability contrast. In the case of $D_p^{in} = 1.2$, we can observe that the droplet spreading is confined to the inner surface only for $\theta_e^{out} = 120^\circ$, i.e. for the variant with the wettability contrast 70°, see Fig. 6(a). Moreover, in the case of $D_p^{in} = 1.4$, the droplet spreading is confined to the inner surface for both $\theta_e^{out} = 90^\circ$ and $\theta_e^{out} = 120^\circ$, i.e. for the variants with wettability contrast 40° and 70°. Hence, the confinement of the droplet within a certain specified area depends on both the wettability contrast and the diameter of inner surface. In the dynamic contact angle curve a sudden shoot at around $t = 1.4$ indicates that the droplet starts to spread in the outer surface. Since the wettability contrast is high in the $\theta_e^{out} = 120^\circ$ case, there are oscillations in the dynamic contact angle at the later stage when the contact line is in the transition region between the inner and outer surface. From the total heat curves, we observe that the total heat transfer from the solid substrate to liquid droplet is maximum for surface with the lowest wettability contrast and higher D_p^{in}. This is due to the fact that the liquid droplet is exposed to a larger surface area, thereby enabling greater heat transfer from the solid substrate to the liquid droplet.

We now present the contours of the magnitude of velocity and the temperature distributions for two variants of impinging droplets, $\theta_e^{out} = 70^\circ$ and 90°, with $\theta_e^{in} = 50^\circ$, $D_p^{in} = 1.4$. Fig. 8 depicts the magnitude of velocity contours in the droplet at different instances t = 0.1, 0.75, 1.5, 2.5 and 5.0. At t = 0.1 and 0.75, the droplet spreading remains similar in both $\theta_e^{out} = 70^\circ$ and 90° variants. However, after $t = 0.75$, θ_e^{out} affects the flow dynamics significantly. We can observe a difference in the magnitude of the velocity at a given time instant. In the variant $\theta_e^{out} = 70^\circ$, the droplet attained its equilibrium but not confined within the inner surface. However, in the case of $\theta_e^{out} = 90^\circ$, the droplet is confined within the inner surface but takes longer time to attain its equilibrium. Fig. 9 depicts the temperature distribution in both the liquid droplet and solid substrate. Initially the dimensionless temperature in the droplet in zero, whereas the temperature in the solid is 1.214 in both variants. The temperature in the droplet increases

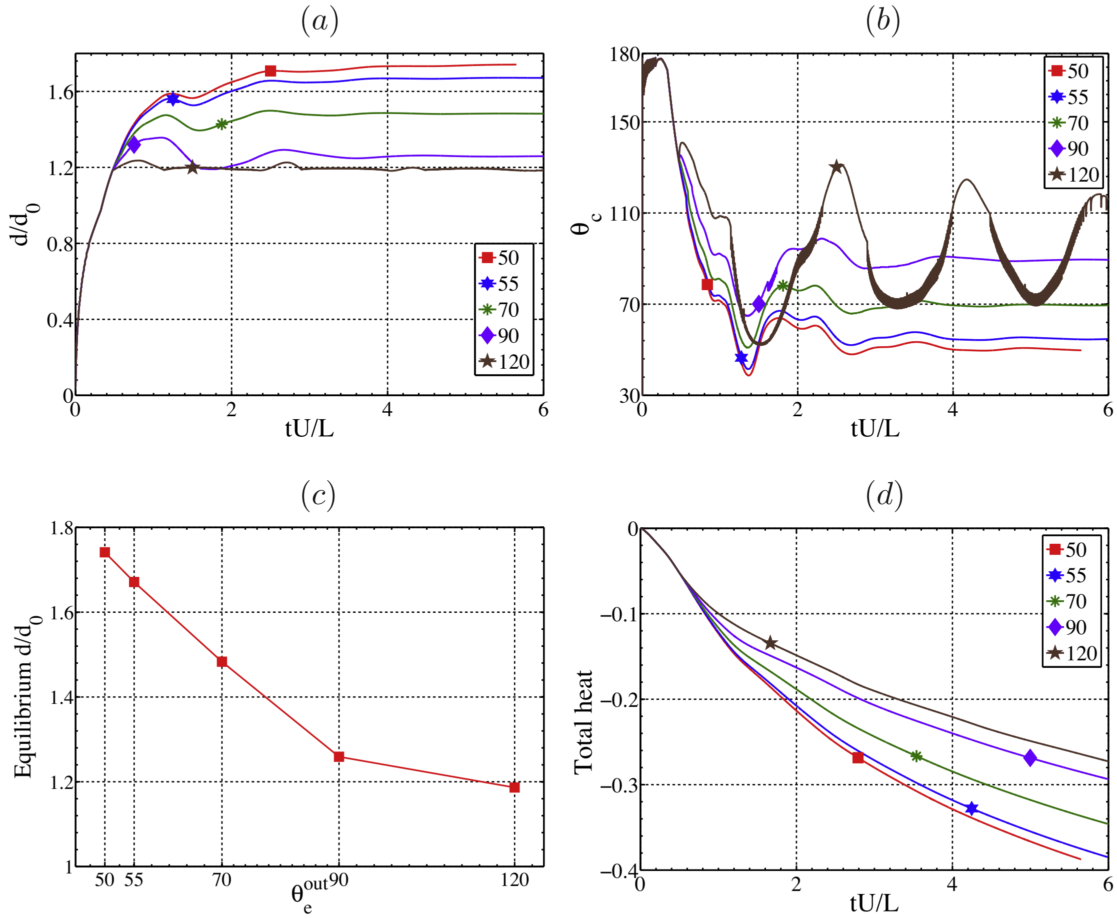

Fig. 6. Wetting diameter (a), dynamic contact angle (b)), equilibrium wetting diameter (c) and total heat (d) of a droplet impinging on a hot solid substrate with diameter of the inner surface $D_p^{in} = 1.2$. Numerical results for (i) $\theta_e^{out} = 50^\circ$, (ii) $\theta_e^{out} = 55^\circ$, (iii) $\theta_e^{out} = 70^\circ$, (iv) $\theta_e^{out} = 90^\circ$ and (v) $\theta_e^{out} = 120^\circ$.

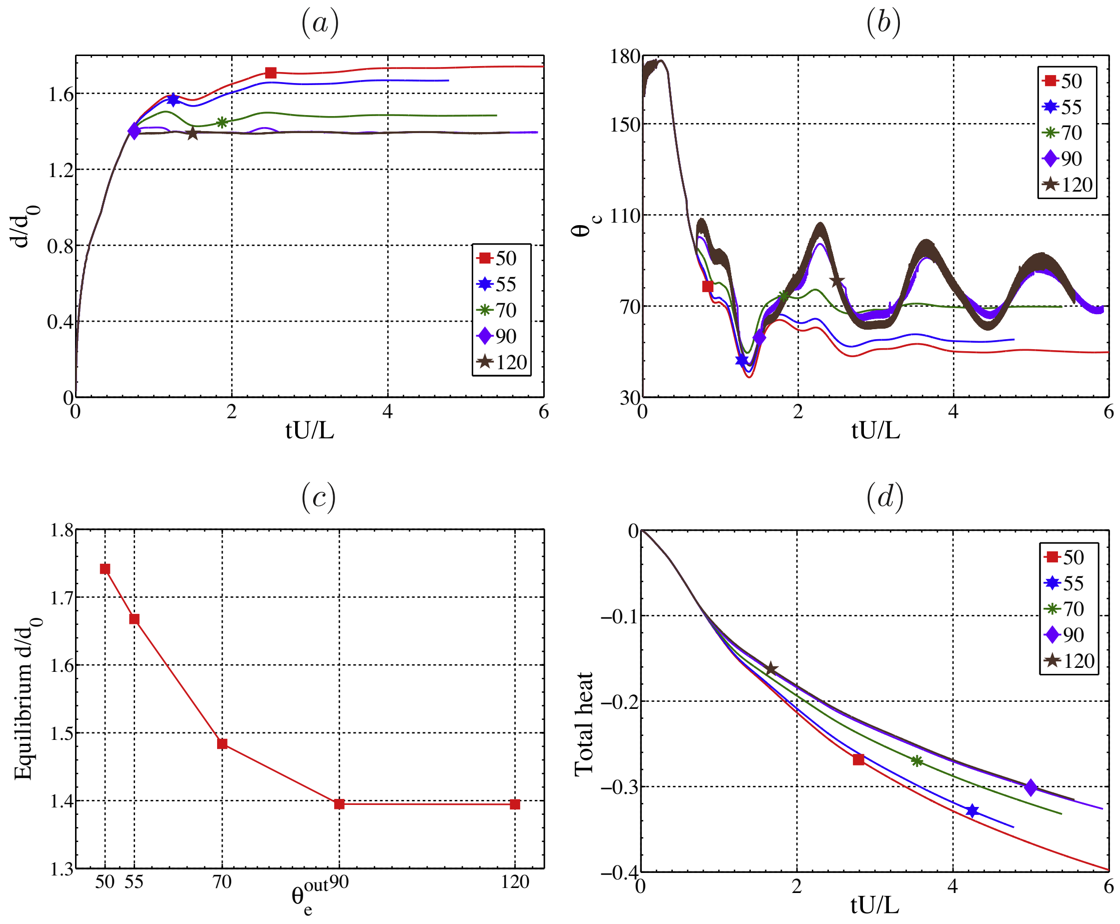

Fig. 7. Wetting diameter (a), dynamic contact angle (b), equilibrium wetting diameter (c) and total heat (d) of a droplet impinging on a hot solid substrate with diameter of the inner surface $D_p^{in} = 1.4$. Numerical results for (i) $\theta_e^{out} = 50^\circ$, (ii) $\theta_e^{out} = 55^\circ$, (iii) $\theta_e^{out} = 70^\circ$, (iv) $\theta_e^{out} = 90^\circ$ and (v) $\theta_e^{out} = 120^\circ$.

with time due to spreading. We have already seen the total heat increases with decrease in θ_e^{out}. The same can also be observed by comparing the minimum temperature in the droplet at a given time instant. Since the droplet is not confined within the inner surface in the variant $\theta_e^{out} = 70^\circ$, it is exposed to a larger surface area, which eventually induce more heat transfer from the solid to liquid.

4.3. Effect of pattern diameter

To study the effect of diameter of a circular patterned solid substrate on the confinement of the spreading droplet, we vary the diameter of the inner surface. We consider the following five variants: (i) $D_p^{in} = 0.8$, (ii) $D_p^{in} = 1.0$, (iii) $D_p^{in} = 1.2$, (iv) $D_p^{in} = 1.4$ and (v) $D_p^{in} = 1.5$. For the above variants we perform two sets of simulations with (1) $\theta_e^{out} = 90^\circ$ and (2) $\theta_e^{out} = 120^\circ$. The contact angle of the inner surface is fixed as $\theta_e^{in} = 50^\circ$. Further, we use the following dimensionless numbers Re = 151, We = 4.5, Fr = 11,125, $\text{Pe}_F = 20$, $\text{Pe}_S = 200$ and Bi = 0.000116 in all variants.

The computationally obtained wetting diameter, dynamic contact angle, equilibrium wetting diameter and the total heat transfer for the above variants are shown in Figs. 10 and 11. From these figures, we can observe that the droplet can be confined to as low as $D_p^{in} = 1.0$, i.e. the initial diameter of the droplet which is quite significant. However, this can be achieved only for the variant $\theta_e^{out} = 120^\circ$. Further, the confinement can be obtained only when $D_p^{in} = 1.4$ and 1.5 for the variant $\theta_e^{out} = 90^\circ$. Moreover, we observe a significant reduction in the equilibrium wetting diameter for the variant $\theta_e^{out} = 120^\circ$ (compared to $\theta_e^{out} = 90^\circ$ variant), see Figs. 10(c) and 11(c). In the dynamic contact angle curves, we observe huge periodic jumps which indicate that the droplet spreads and recoils in the transition region.

From the total heat curves, we observe that the total heat transfer from the solid substrate to the liquid droplet is maximum for surface with the higher inner diameter which enables larger surface area for heat transfer. Till now, we have analyzed the spreading and confinement of droplet on a circular patterned heterogeneous surface for fixed material properties of the liquid. In the subsequent sections we study the effect of Reynolds number and Weber number on the confinement of the droplet spreading.

4.4. Effect of Reynolds number

In this section we perform a comprehensive study of the effect of Reynolds number on the spreading and confinement of droplet on a circular patterned heterogeneous solid substrate. We consider a water droplet with the same material properties as in the mesh convergence study, and it results in We = 4.5, Fr = 11,125, $\text{Pe}_F = 20$, Pe_S = 200 and Bi = 0.000116. The contact angle of inner surface is fixed as $\theta_e^{in} = 50^\circ$. In order to study the influence of Reynolds number, we consider six variants: (i) Re = 40, (ii) Re = 75, (iii) Re = 150, (iv) Re = 300, (v) Re = 600 and (vi)

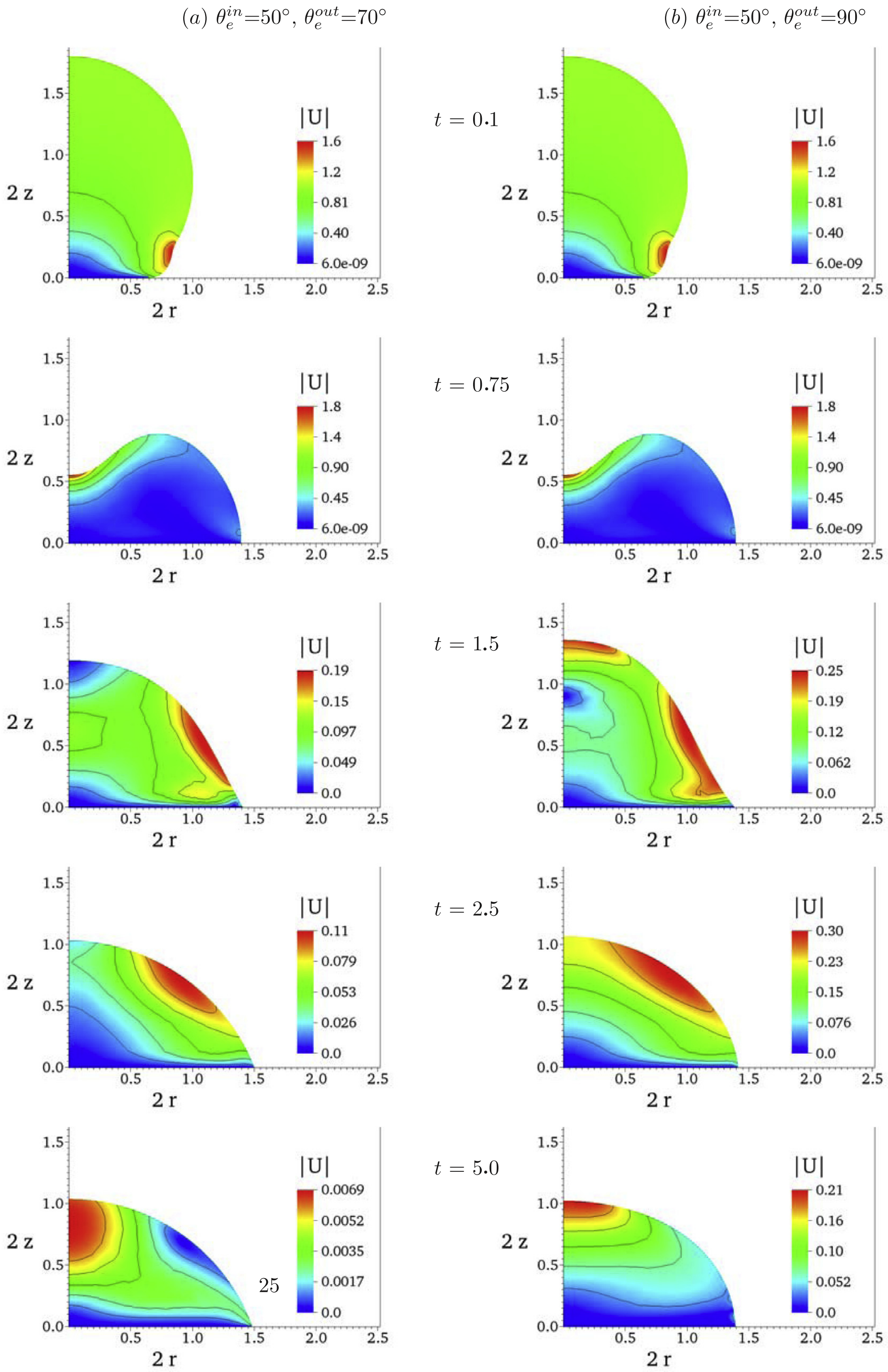

Fig. 8. Velocity (magnitude) contours of an impinging droplet with $\theta_e^{in} = 50^\circ$, $D_p^{in} = 1.4$ at dimensionless time t = 0.1, 0.75, 1.5, 2.5, 5.0 from the top for (a) $\theta_e^{out} = 70^\circ$ (left column) and (b) $\theta_e^{out} = 90^\circ$ (right column).

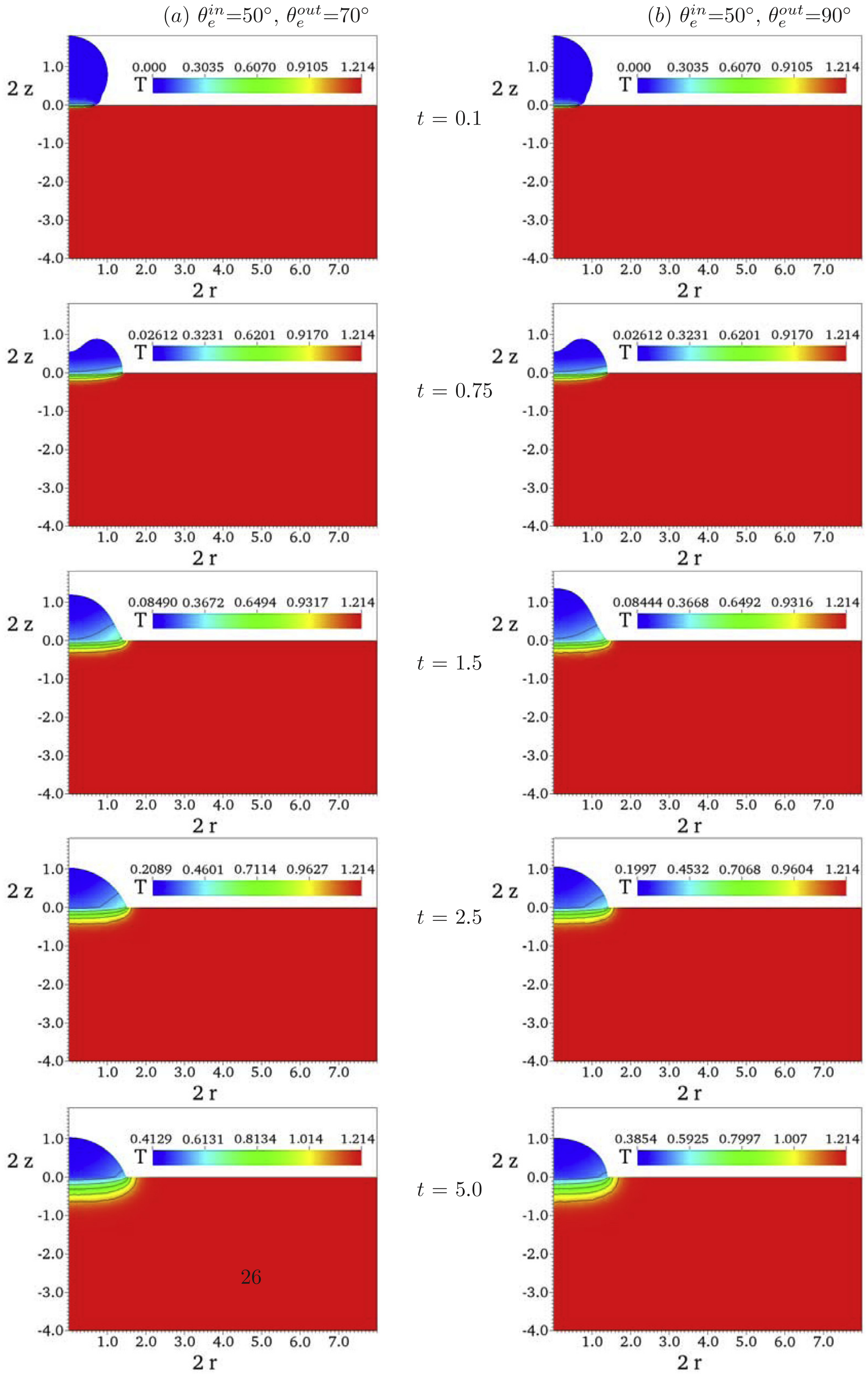

Fig. 9. Temperature contours of an impinging droplet with $\theta_e^{in} = 50^\circ$, $D_p^{in} = 1.4$ at dimensionless time t = 0.1, 0.75, 1.5, 2.5, 5.0 from the top for (a) $\theta_e^{out} = 70^\circ$ (left column) and (b) $\theta_e^{out} = 90^\circ$ (right column).

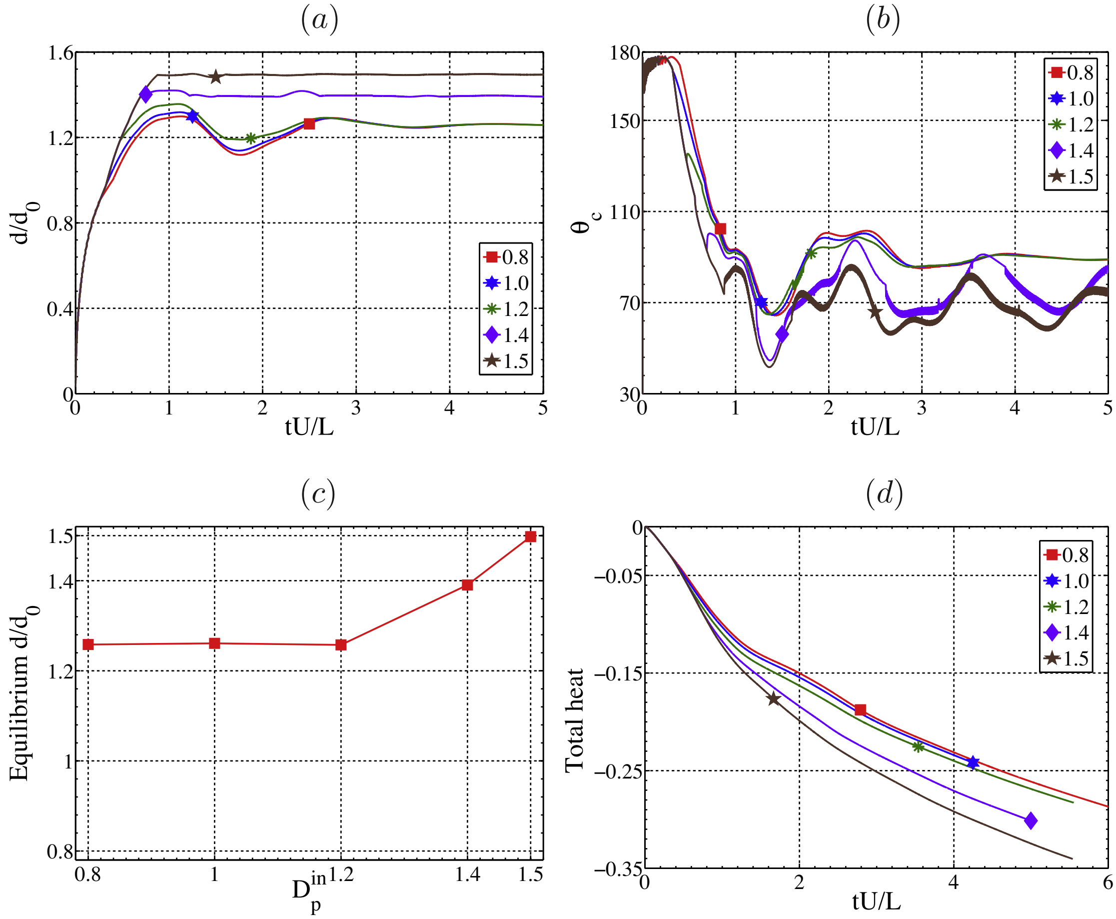

Fig. 10. Wetting diameter (a), dynamic contact angle (b), equilibrium wetting diameter (c) and total heat (d) of a droplet impinging on a hot solid substrate with $\theta_e^{out} = 90^\circ$. Numerical results for (i) $D_p^{in} = 0.8$, (ii) $D_p^{in} = 1.0$, (iii) $D_p^{in} = 1.2$, (iv) $D_p^{in} = 1.4$ and (v) $D_p^{in} = 1.5$.

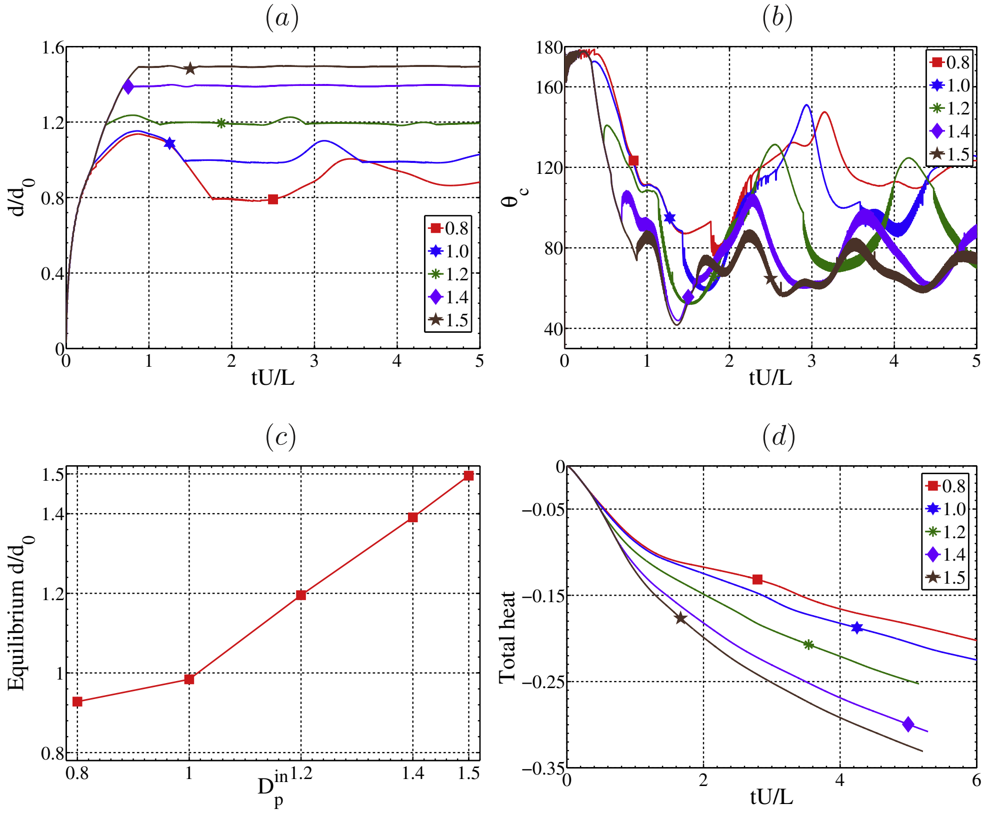

Fig. 11. Wetting diameter (a), dynamic contact angle (b), equilibrium wetting diameter (c) and total heat (d) of a droplet impinging on a hot solid substrate with outer $\theta_e^{out} = 120^\circ$. Numerical results for (i) $D_p^{in} = 0.8$, (ii) $D_p^{in} = 1.0$, (iii) $D_p^{in} = 1.2$, (iv) $D_p^{in} = 1.4$ and (v) $D_p^{in} = 1.5$.

Re = 1200 by varying the viscosity. The slip numbers for these variants are chosen based on the relation proposed in [23]. Two sets of simulations with (1) $\theta_e^{out} = 90^\circ$ and (2) $\theta_e^{out} = 120^\circ$ are performed for the above variants.

We first consider the case, $D_p^{in} = 1.0$, and the computationally obtained wetting diameter, dynamic contact angle, maximum wetting diameter and the total heat transfer for the above variants are shown in Figs. 12 and 13. The choice $D_p^{in} = 1.0$ implies that the aim is to confine the impinging droplet spreading to the inner region, which is equal to the initial diameter of the droplet. Confinement can be achieved for the variant $\theta_e^{out} = 120^\circ$ but the same is not true in $\theta_e^{out} = 90^\circ$. However, the interesting observation is the effect of Reynolds number, i.e. the effect of the viscosity of the liquid on the confinement. The maximum wetting diameter increases with increase in the Reynolds number, but the Reynolds number does not affect the equilibrium wetting diameter which can be seen in Fig. 12(a) and (c). Since the equilibrium wetting diameter remains the same, we can confine the droplet within a certain specified circular region irrespective of the Reynolds number. However, the maximum wetting diameter needs to be confined within a specified region in certain applications. It can be achieved by choosing a liquid with appropriate viscosity, see Fig. 13(a) and (c). We can also observe that the maximum wetting diameter can be scaled down by 10–15% in $\theta_e^{out} = 120^\circ$ and less than 10% in $\theta_e^{out} = 90^\circ$ with an appropriate choice of viscosity. However, it is appropriate to choose a higher wettability contrast for further reducing the maximum wetting diameter. The dynamic contact angle over time oscillates as the droplet spreads and recoils over the inner and outer surface. Due to the frequent transition of the contact line between the inner and outer surface and vice-verse, we observe oscillations in the dynamic contact angle when the wettability contrast is more. The total heat transfer from the solid substrate to the liquid droplet is directly proportional to the wetting area of the liquid. Hence, from Fig. 13(b) and (d), we can observe that the total heat transfer is less in the variant Re = 40. The total heat transfer is almost same for high Reynolds number cases, and it is due to the confinement of droplet within the inner region.

Figs. 14 and 15 present the numerical results for the case $D_p^{in} = 1.4$. From Fig. 14(a) and (c), we can observe that the droplet is confined to the inner region in both variants, $\theta_e^{out} = 90^\circ$ and $\theta_e^{out} = 120^\circ$. Fig. 14(b) and (d) shows oscillations in the dynamic contact angle which indicate that the contact line is in the transition region. Fig. 15 shows the maximum wetting diameter and the total heat transfer. We observe almost the same scaling down of the maximum wetting diameter in the variant $\theta_e^{out} = 90^\circ$ as observed previously in the case $D_p^{in} = 1.0$. Moreover, it is interesting to note that the maximum wetting diameter is confined within the inner region irrespective of the Reynolds number in the variant, $\theta_e^{out} = 120^\circ$. From Fig. 15(b) and (d), we can observe that the total heat transfer is less in the variant Re = 40. The total heat transfer is almost the same when the Reynolds number is high due to the confinement of the droplet within the inner region.

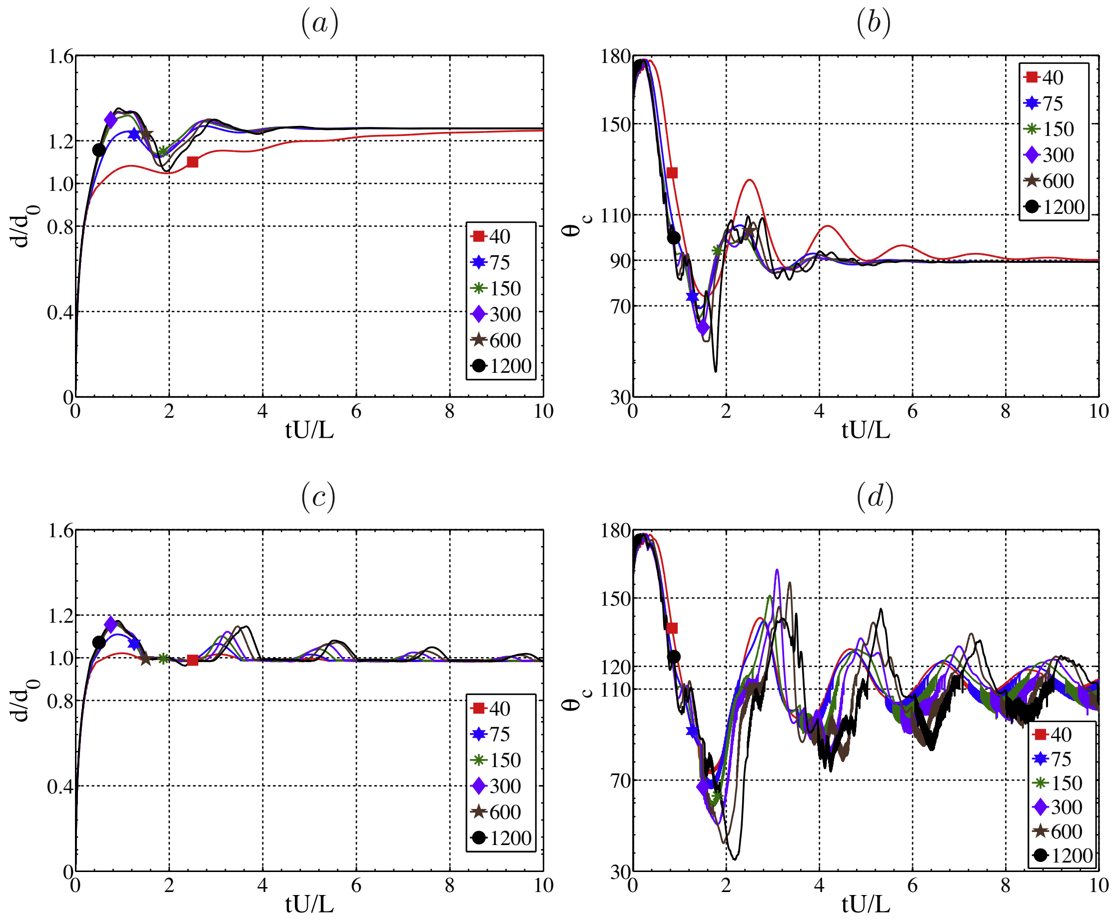

Fig. 12. Wetting diameter (a), (c) and dynamic contact angle (b), (d) of droplet impinging on a hot solid substrate with $D_p^{in} = 1.0$ for two test cases: $\theta_e^{out} = 90^\circ$ (a), (b) and $\theta_e^{out} = 120^\circ$ (c), (d). Numerical results for (i) Re = 40, (ii) Re = 75, (iii) Re = 150, (iv) Re = 300, (v) Re = 600 and (vi) Re = 1200.

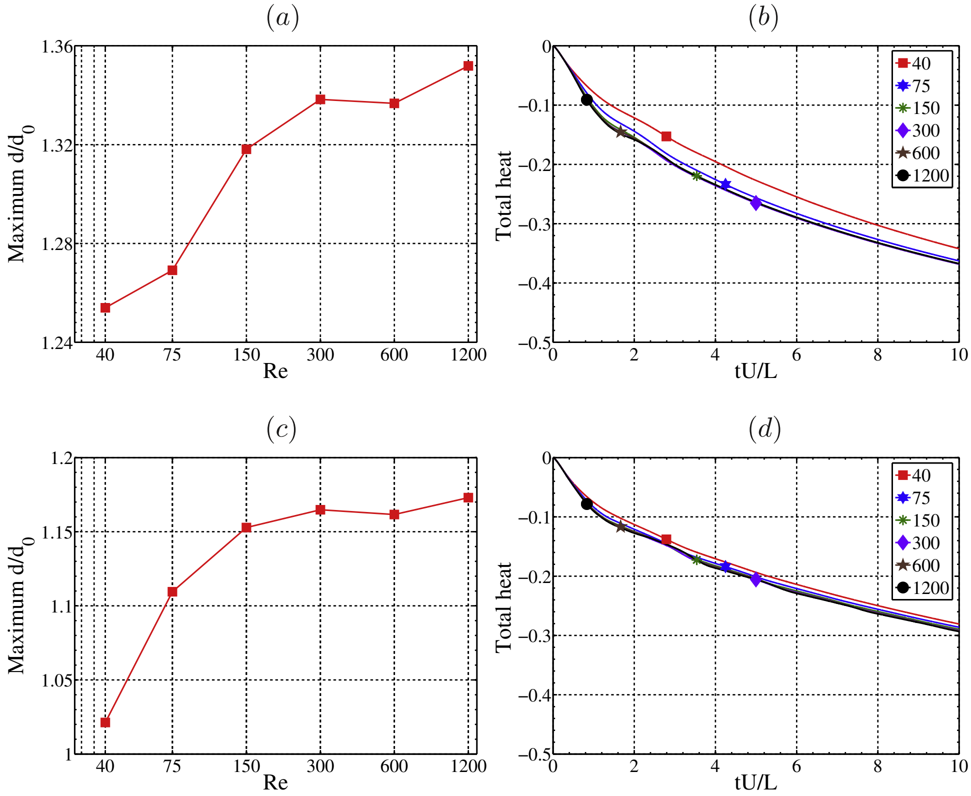

Fig. 13. Maximum wetting diameter (a), (c) and total heat (b), (d) of droplet impinging on a hot solid substrate with $D_p^{in} = 1.0$ for two test cases: $\theta_e^{out} = 90^\circ$ (a), (b) and $\theta_e^{out} = 120^\circ$ (c), (d). Numerical results for (i) Re = 40, (ii) Re = 75, (iii) Re = 150, (iv) Re = 300, (v) Re = 600 and (vi) Re = 1200.

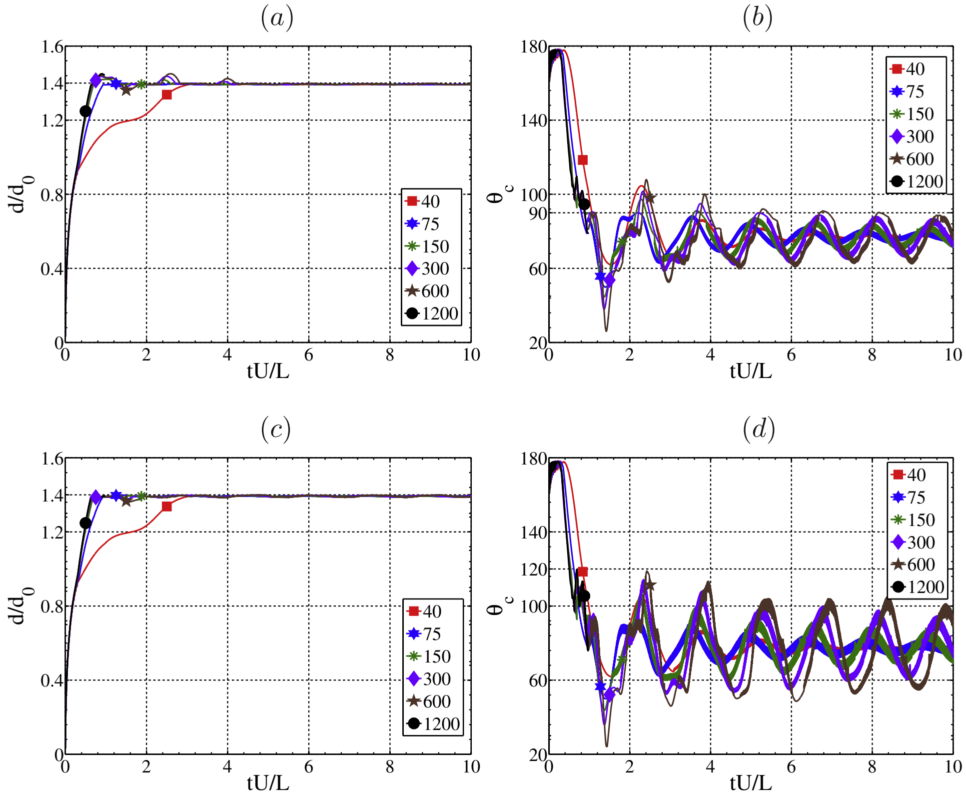

Fig. 14. Wetting diameter (a), (c) and dynamic contact angle (b), (d) of droplet impinging on a hot solid substrate with $D_p^{in} = 1.4$ for two test cases: $\theta_e^{out} = 90^\circ$ (a), (b) and $\theta_e^{out} = 120^\circ$ (c), (d). Numerical results for (i) Re = 40, (ii) Re = 75, (iii) Re = 150, (iv) Re = 300, (v) Re = 600 and (vi) Re = 1200.

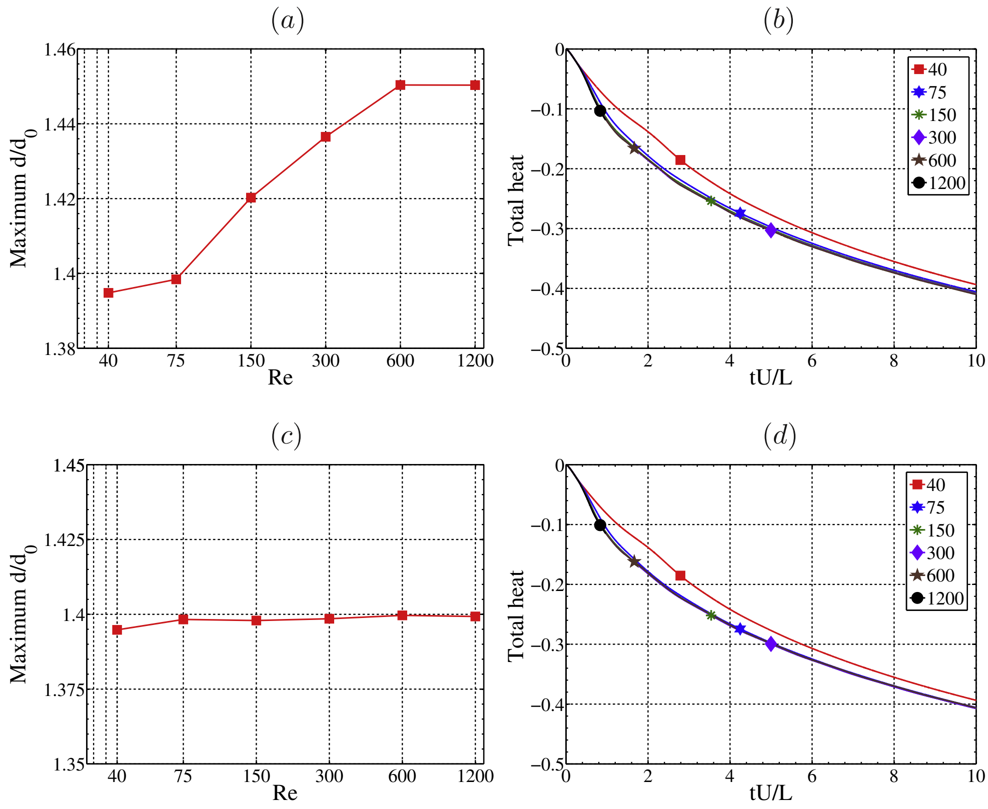

Fig. 15. Maximum wetting diameter (a), (c) and total heat (b), (d) of droplet impinging on a hot solid substrate with $D_p^{in} = 1.4$ for two test cases: $\theta_e^{out} = 90^\circ$ (a), (b) and $\theta_e^{out} = 120^\circ$ (c), (d). Numerical results for (i) Re = 40, (ii) Re = 75, (iii) Re = 150, (iv) Re = 300, (v) Re = 600 and (vi) Re = 1200.

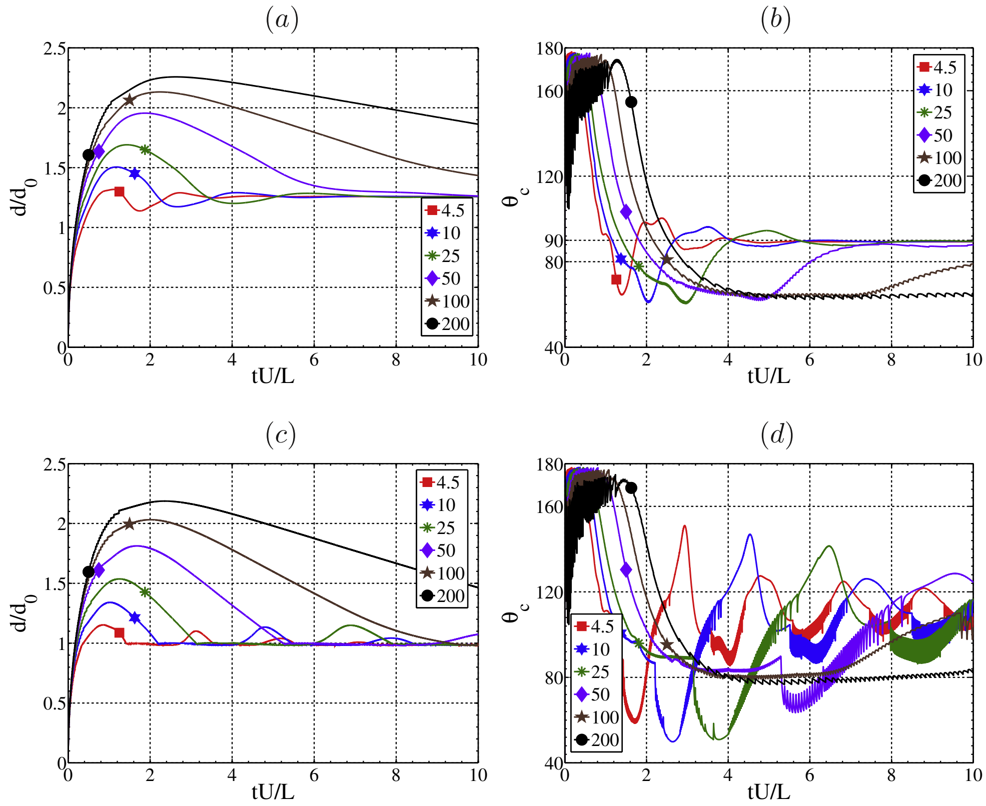

Fig. 16. Wetting diameter (a), (c) and dynamic contact angle (b), (d) of droplet impinging on a hot solid substrate with $D_p^{in} = 1.0$ for two test cases: $\theta_e^{out} = 90^\circ$ (a), (b) and $\theta_e^{out} = 120^\circ$ (c), (d). Numerical results for (i) We = 4.5, (ii) We = 10, (iii) We = 20, (iv) We = 50, (v) We = 100 and (vi) We = 200.

4.5. Effect of Weber number

In this section we study the effect of the Weber number on the spreading and confinement of droplet on a solid substrate with circular patterned heterogeneous wettability. We consider a water droplet with the same material properties as in the mesh convergence study with Re = 75.5, Fr = 11,125, $\mathrm{Pe}_F = 20$, $\mathrm{Pe}_S = 200$ and Bi = 0.000116. The contact angle of inner surface is fixed as $\theta_e^{in} = 50^\circ$. In order to study the influence of the Weber number, we consider six variants: (i) We = 4.5, (ii) We = 10, (iii) We = 20, (iv) We = 50, (v) We = 100 and (vi) We = 200 by varying the surface tension. The slip numbers are chosen as proposed in [23]. We perform two sets of simulations for the above variants with (1) $\theta_e^{out} = 90^\circ$ and (2) $\theta_e^{out} = 120^\circ$.

We first consider the case, $D_p^{in} = 1.0$, and the computationally obtained wetting diameter, dynamic contact angle, maximum wetting diameter and the total heat transfer for the above variants are shown in Figs. 16 and 17. Confinement of the droplet within the inner region is achieved in the variant, $\theta_e^{out} = 120^\circ$, however, the same is not true in the variant, $\theta_e^{out} = 90^\circ$. Further, the maximum wetting diameter increases with an increase in the Weber number, but the Weber number does not affect the equilibrium wetting diameter, which can be seen in Fig. 16(c). Since the equilibrium wetting diameter remains the same, we can confine the droplet within a certain circular region irrespective of the Weber number. However, the maximum wetting diameter needs to be confined within a specified region in certain applications and it can be achieved by choosing a liquid with appropriate surface tension, see Fig. 17(a) and (c). Oscillations are observed in the dynamic contact angle curves, and it indicate that the contact line is in the transition region, see Fig. 16(d). Further, Fig. 17(b) and (d) shows the total heat transfer. The total heat transfer from the solid substrate to the liquid droplet is directly proportional to the wetting area of the liquid. Hence, more total heat transfer is observed when the Weber number is high. Interestingly, the difference between the effects of Reynolds and Weber number on the total heat transfer is quite significant. In the case of increase in the Reynolds number, the maximum wetting diameter increases only about 10% for the considered values of the Reynolds number. However, the maximum wetting diameter increases about 40–100% when the Weber number is increased.

The numerical results for the case, $D_p^{in} = 1.4$ are shown in Figs. 18 and 19. We can observe that the droplet is confined within the inner region irrespective of the Weber number in both variants, $\theta_e^{out} = 90^\circ$ and 120°. Further, oscillations are observed in the dynamic contact angle curve when the contact line is in the transition region. Moreover, we can observe that the wettability contrast has negligible effect on the variation of maximum wetting diameter with Weber number, since the droplet is confined within the inner region in both variants, $\theta_e^{out} = 90^\circ$ and 120° see Fig. 19(a) and (c). From the total heat curves, we can observe that the total heat increases with increase in the Weber number, see Fig. 19(b) and (d).

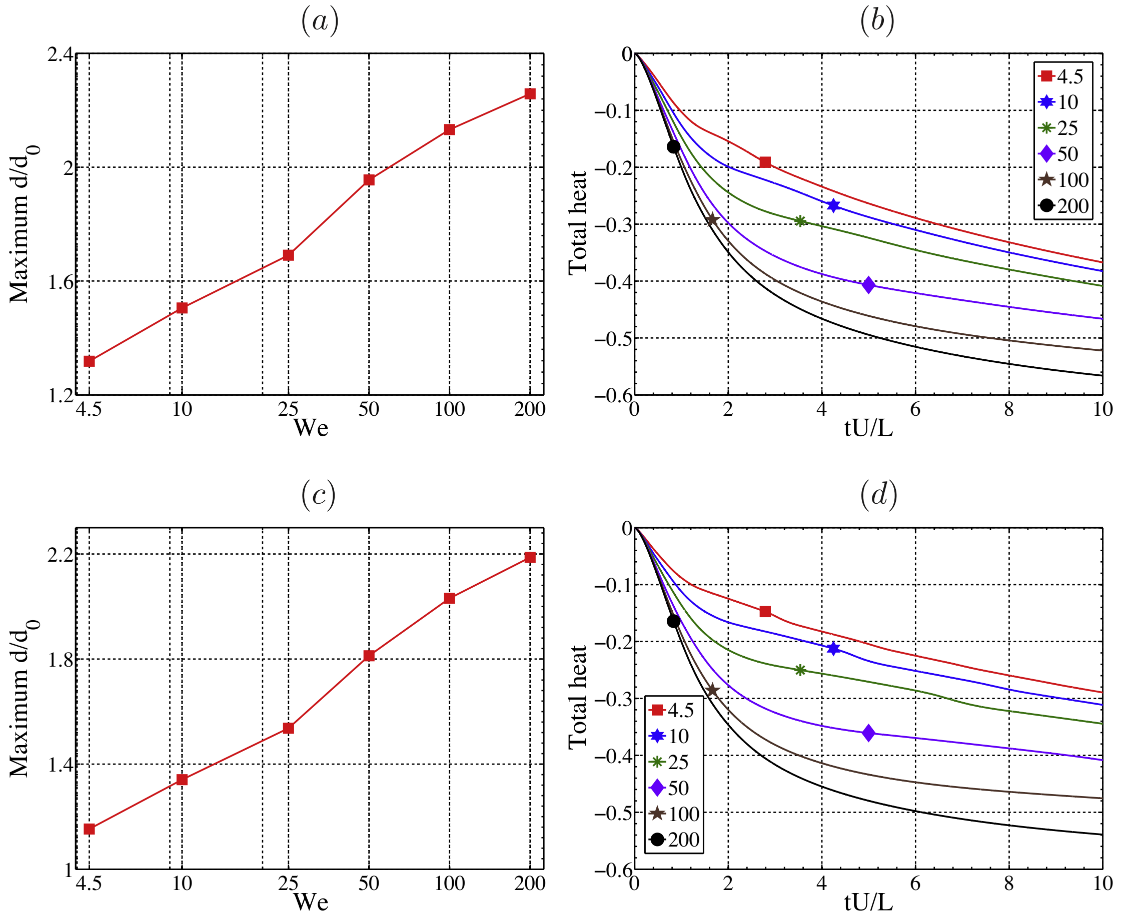

Fig. 17. Maximum wetting diameter (a), (c) and total heat (b), (d) of droplet impinging on a hot solid substrate with $D_p^{in} = 1.0$ for two test cases: $\theta_e^{out} = 90^\circ$ (a), (b) and $\theta_e^{out} = 120^\circ$ (c), (d). Numerical results for (i) We = 4.5, (ii) We = 10, (iii) We = 20, (iv) We = 50, (v) We = 100 and (vi) We = 200.

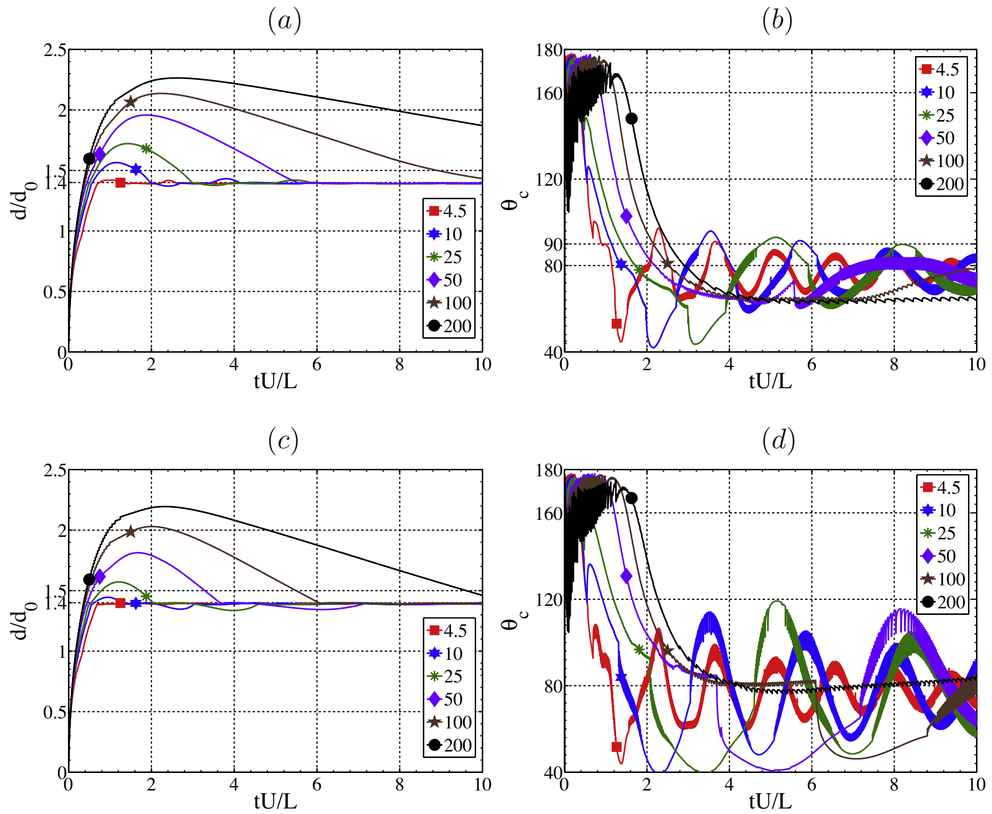

Fig. 18. Wetting diameter (a), (c) and dynamic contact angle (b), (d) of droplet impinging on a hot solid substrate with $D_p^{in} = 1.4$ for two test cases: $\theta_e^{out} = 90^\circ$ (a), (b) and $\theta_e^{out} = 120^\circ$ (c), (d). Numerical results for (i) We = 4.5, (ii) We = 10, (iii) We = 20, (iv) We = 50, (v) We = 100 and (vi) We = 200.

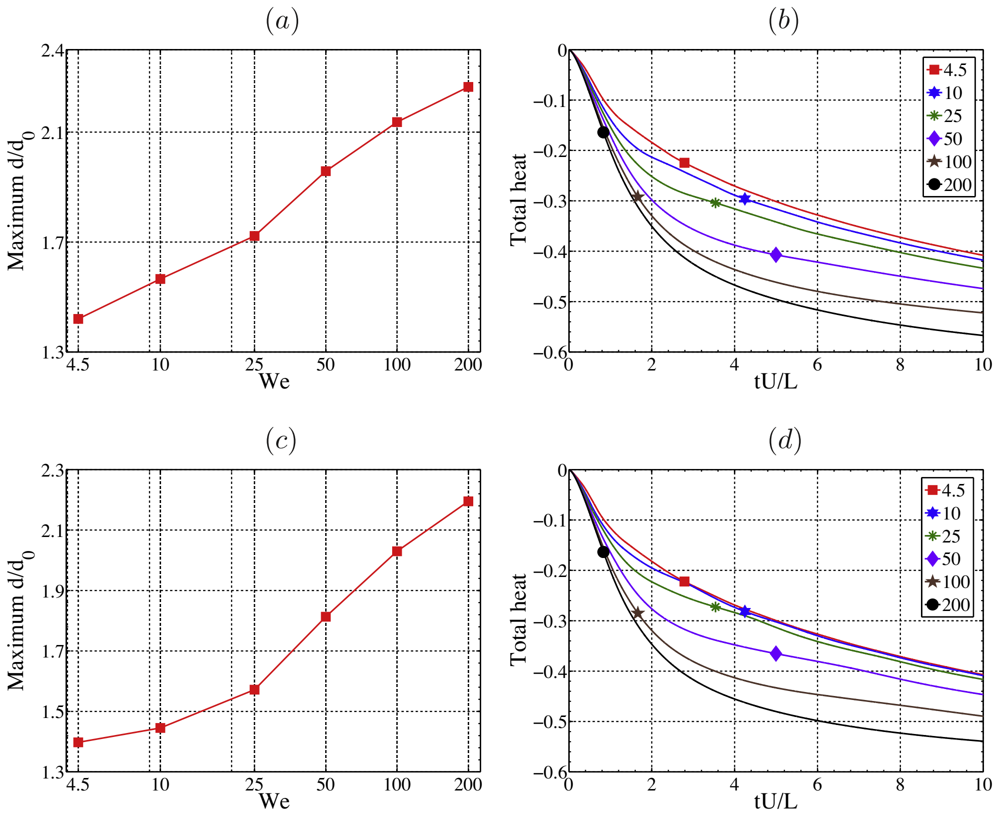

Fig. 19. Maximum wetting diameter (a), (c) and total heat (b), (d) of droplet impinging on a hot solid substrate with $D_p^{in} = 1.4$ for two test cases: $\theta_e^{out} = 90^\circ$ (a), (b) and $\theta_e^{out} = 120^\circ$ (c), (d). Numerical results for (i) We = 4.5, (ii) We = 10, (iii) We = 20, (iv) We = 50, (v) We = 100 and (vi) We = 200.

5. Summary

A finite element scheme using the ALE approach is presented for the simulations of a non-isothermal liquid droplet impinging on a heated solid substrate with circular patterned heterogeneous wettability. In this study, the inner region is assumed to be more wettable than the outer region, and this heterogeneous wettability is incorporated into the model using a space-dependent contact angle. A mesh convergence study is first performed and then the numerical scheme is validated with experimental results from literature. Further, the mass and the internal energy fluctuations in the entire simulations are less than one percent, and it shows the accuracy of the numerical scheme. An array of numerical simulations are performed to study the effects of the wettability contrast, pattern diameter, Reynolds number and Weber number on the confinement of the droplet spreading. In all test cases, the total heat transfer from the solid substrate to the liquid droplet is also examined.

The following points are observed from the numerical simulations. The confinement of the droplet within a specified area depends on the wettability contrast and the diameter of the inner surface. Further, the maximum wetting diameter increases with an increase in the Reynolds number and Weber number. In certain applications, controlling the maximum wetting diameter is crucial when the maximum allowable wetting area is prescribed. It can be achieved by choosing a liquid with appropriate viscosity and/or surface tension. Moreover, the influence of the Reynolds number on the maximum wetting diameter is negligible in comparison to the Weber number. Next, the total heat transfer from the solid substrate to the liquid droplet is more when the diameter of inner surface is large and/or the wettability contrast is less since $\theta_e^{in} \leqslant \theta_e^{out}$. Further, the influence of the Weber number on the total heat transfer is more compared to the Reynolds number.

References

[1] D. Xia, L.M. Johnson, G.P. López, Anisotropic wetting surfaces with one-dimensional and directional structures: fabrication approaches, wetting properties and potential applications, Adv. Mater. 24 (2012) 1287–1302.

[2] S. Brandon, A. Wachs, A. Marmur, Simulated contact angle hysteresis of a three-dimensional drop on a chemically heterogeneous surface: a numerical example, J. Colloid Interface Sci. 191 (1) (1997) 110–116.

[3] S.D. Iliev, N.C. Pesheva, Wetting properties of well-structured heterogeneous substrates, Langmuir 19 (2003) 9923–9931.

[4] M. Iwamatsu, Contact angle hysteresis of cylindrical drops on chemically heterogeneous stripes surfaces, J. Colloid Interface Sci. 297 (2006) 772–777.

[5] H.P. Jansen, O. Bliznyuk, E.S. Kooij, B. Poelsema, H.J.W. Zandvliet, Simulating anisotropic droplet shapes on chemically striped patterned surfaces, Langmuir 28 (1) (2012) 499–505.

[6] H. Kusumaatmaja, J. Leopoldes, A. Dupuis, J.M. Yeomans, Drop dynamics on chemically patterned surfaces, Europhys. Lett. 73 (5) (2006) 740–746.

[7] M. Lundgren, N.L. Allan, T. Cosgrove, Modeling of wetting: a study of nanowetting at rough and heterogeneous surfaces, Langmuir 23 (3) (2007) 1187–1194.

[8] C.Y. Lim, Y.C. Lam, Phase-field simulation of impingement and spreading of micro-sized droplet on heterogeneous surface, Microfluid. Nanofluid. 13 (2014) 131–148.

[9] H. Fujimoto, N. Hatta, Deformation and rebounding processes of a water droplet impinging on a flat surface above Leidenfrost temperature, J. Fluids Eng. 118 (1996) 142–149.

[10] M. Pasandideh-Fard, R. Bhola, S. Chandra, J. Mostaghimi, Deposition of tin droplets on a steel plate: simulations and experiments, Int. J. Heat Mass Transfer 41 (1998) 2929–2945.

[11] M. Francois, W. Shyy, Computations of drop dynamics with the immersed boundary method. Part 2: Drop impact and heat transfer, Numer. Heat Trans., Part B: Fundam. 44 (2) (2003) 119–143.

[12] J.F.Z. Zhao, D. Poulikakos, Heat transfer and fluid dynamics during the collision of a liquid droplet on a substrate. 1: Modeling, Int. J. Heat Mass Transfer 39 (13) (1996) 2771–2789.

[13] L.S.F.Y. Ge, 3-D modeling of the dynamics and heat transfer characteristics of subcooled droplet impact on a surface with film boiling, Int. J. Heat Mass Transfer 49 (21–22) (2006) 4231–4249.

[14] G. Strotos, M. Gavaises, A. Theodorakakos, G. Bergeles, Numerical investigation of the cooling effectiveness of a droplet impinging on a heated surface, Int. J. Heat Mass Transfer 51 (19–20) (2008) 4728–4742.

[15] A. Briones, J.S. Ervin, S.A. Putnam, L.W. Byrd, L. Gschwender, Micrometer-sized water droplet impingement dynamics and evaporation on a flat dry surface, Langmuir 26 (16) (2010) 13272–13286.

[16] S.A. Putnam, A.M. Briones, L.W. Byrd, J.S. Ervin, M.S. Hanchak, A. White, J.G. Jones, Microdroplet evaporation on superheated surfaces, Int. J. Heat Mass Transfer 55 (21–22) (2012) 5793–5807.

[17] S. Ganesan, S. Rajasekaran, L. Tobiska, Numerical modeling of the non-isothermal liquid droplet impact on a hot solid substrate, Int. J. Heat Mass Transfer 78 (2014) 670–687.

[18] S. Ganesan, L. Tobiska, A coupled arbitrary Lagrangian–Eulerian and Lagrangian method for computation of free surface flows with insoluble surfactants, J. Comput. Phys. 228 (8) (2009) 2859–2873.

[19] S. Ganesan, L. Tobiska, Arbitrary Lagrangian–Eulerian finite-element method for computation of two-phase flows with soluble surfactants, J. Comput. Phys. 231 (9) (2012) 3685–3702.

[20] S. Turek, Efficient solvers for incompressible flow problems, An algorithmic and computational approach, Springer-Verlag, Berlin, 1999.

[21] S. Ganesan, L. Tobiska, An accurate finite element scheme with moving meshes for computing 3D-axisymmetric interface flows, Int. J. Numer. Methods Fluids 57 (2) (2008) 119–138.

[22] V. Girault, P.-A. Raviart, Finite Element Methods for Navier–Stokes equations, Springer-Verlag, Berlin, Heidelberg, New York, 1986.

[23] S. Ganesan, J. Venkatesan, Mesh-dependent slip for computations of impinging droplets with sharp interface methods, 2015, pp. 1–19, Available from: <arXiv: 1502.04884>.